Department of Environment Systems
Graduate School of Frontier Sciences
The University of Tokyo

2023

Master's Thesis

ROCK PHYSICS CONSIDERATION OF DYNAMIC FRICTION IN METHANE HYDRATE BEARNG SEDIMENTS AS ONE OF MECHANISMS OF S-WAVE ATTENUATION

（メタンハイドレート堆積物における S 波減衰機構の一つとしての
動摩擦に関する岩石物理学的検討）

Submitted August 16, 2023

Adviser: Professor Jun Matsushima
Co-Adviser: Masaatsu Aichi

牛梓函

TABLE OF CONTENTS

ABSTRACT **1**

CHAPTER 1. INTRODUCTION **3**

CHAPTER 2. METHOD **15**

2.1 Workflows **15**

2.2 Representative element volume (REV) **17**

2.3 Static analysis **18**

2.4 Dynamic analysis **28**

2.5 Spectrum analysis **32**

2.6 Input parameters **33**

CHAPTER 3. RESULTS **38**

CHAPTER 4. DISCUSSION **40**

CHAPTER 5. CONCLUSIONS **42**

ACKNOWLEDGEMENTS **43**

APPENDIX **44**

REFERENCES **46**

ABSTRACT

The dissociation of methane hydrate (MH) accumulations can trigger submarine slope failures or sediment slumps. Geophysical exploration plays a crucial role in the identification and characterization of sediment formations containing MH. Among the various geophysical techniques, seismic methods are widely used for MH detection and characterization. Recent advances in various types of seismic measurement methods such sonic logging, vertical seismic profiling (VSP), and surface seismic survey allow P- and S-wave attenuation to be measured at a broadband frequency range. Recent S-wave attenuation estimation in methane hydrate bearing sediments shows low frequency dependence between sonic logging and seismic exploration frequencies. However, existing rock physics models cannot explain such frequency independence and further underestimate the magnitude of S-wave attenuation. To fill the gap between observed and theoretical S-wave attenuation values, this study formulates a rock physics model that integrates dynamic friction on the contact lines as a contributing mechanism for S-wave attenuation. A representative element volume (REV) model is used to simulate the structure of the sediments, this model can reflect the effect of contact line well. Then the *Kolosov-Muskhelishvili potentials* method is used to calculate the displacement of every point in the 2-dimentional plane under certain liquid pressure and far-field stress. Finally, a stepping system is constructed to simulate the periodic variation when the S-wave propagates the REV, and calculate the attenuation. The simulation results show that the friction occurring at the three-phase contact line between methane hydrate, sand grains, and seawater engenders considerable dissipation. Also, the shear wave attenuation predicted by this model fits well with the attenuation estimated from walkaway vertical seismic profiling (w-VSP) exploration data, and exhibits low frequency dependency. Although the proposed method is highly related to the range of contact angle, we draw the

conclusion that the dynamic friction on the contact line might be the main mechanism of shear wave attenuation.

Key words: methane hydrate bearing sediments, S-wave attenuation, rock physics modeling, frequency dependence, contact line

CHAPTER 1. INTRODUCTION

Gas hydrate is a crystalline compound formed through the combination of water and guest molecules under specific conditions of high pressure and low temperature (Sloan & Koh, 2007). Methane hydrate (MH) specifically refers to gas hydrate where methane is the guest molecule and water molecules form the crystal lattice structure. MH holds great potential as an alternative energy source and possesses significant implications for global climate change and sub-marine geohazards (Haq, 1999). The discovery of MH accumulations in permafrost regions and beneath the ocean along continental margins has sparked considerable interest in MH as an unconventional and promising energy resource for the future (Kelland, 1994). The attractiveness of MH as an energy resource stems from two key factors: the vast quantities of methane within MH accumulations and the widespread distribution of sediments hosting MH (Kvenvolden, 1993). Notably, Demirbas (2010) estimated that the methane content in MH reaches approximately 2×10^{16} m^3, surpassing the collective volume of conventional fossil fuels.

In addition to its potential as an unconventional energy resource, methane hydrate (MH) also has implications for global climate change and submarine geohazards (Boswell & Collett, 2011; Dawe & Thomas, 2007). The large-scale dissociation of MH can contribute to enhanced warming if released methane reaches the atmosphere, and it can also occur as a consequence of warming due to changes in sea level (pressure) and ocean temperature, affecting the stability conditions of intermediate-pressure and low-temperature environments (Ruppel & Kessler, 2017).

Furthermore, the dissociation of MH accumulations can trigger submarine slope failures or sediment slumps (Paull, 2001; Kvenvolden, 1993; Maslin et al., 2010; McIver, 1977; Paull et al., 2002; Paull et al., 2007). Changes in sea level or ocean bottom topography can disrupt the stability

conditions necessary for MH formation, leading to its dissociation. This release of methane into the ocean column can result in submarine sediment slumps and slides.

Geophysical exploration plays a crucial role in the identification and characterization of sediment formations containing methane hydrate (MH), including parameters such as hydrate saturation, lithology, permeability, porosity, and the extent and thickness of MH-bearing sediments (Boswell & Collett, 2011). Among the various geophysical techniques, seismic methods are widely used for MH detection. In marine environments, the seismic reflection profile is commonly employed to identify the base of the MH stability zone, known as the Bottom Simulating Reflector (BSR) (Holbrook et al., 1996). By deploying seismic receivers on the ocean floor, such as ocean bottom seismometers (OBS), accurate analysis of velocity and geological structures can be conducted. This approach has been successfully applied in several locations with known MH occurrences (Hobro et al., 2005; Petersen et al., 2007; Riedel et al., 2010). Rock physics modeling allows the estimation of seismic velocity based on seismic data, which can be correlated with hydrate saturation. Hence, the assessment of MH reservoirs, including their structure, thickness, and lateral extent, can be enhanced (Dai et al., 2012). However, it is important to note that determining hydrate saturation solely from P- and S-wave velocities in MH-bearing sediments remains challenging due to the strong influence of sediment composition, porosity, and hydrate morphology on velocity measurements.

In this research, sonic and VSP (Vertical Seismic Profiling) data were collected in the Nankai Trough, which is situated beneath the Pacific Ocean off the southeastern coast of Japan. The Japanese Ministry of International Trade and Industry (MITI) drilled a total of six wells in this region, including a main well, two pilot wells, and three post-survey wells, with a narrow spacing of 10-100 meters. Detailed information regarding the drilling program and geological context of

this area can be found in the works of Tsuji et al. (2004) and Uchida et al. (2004). For the present study, the wireline logging and VSP data from two of the post-survey wells (PSW1 and PSW3) were selected due to their high quality (Matsushima 2005, 2006).

Matsushima & Zhan (2020) compared the S-wave attenuation values from sonic log waveform data (Suzuki & Matsushima, 2013) and the attenuation values derived from the walkaway vertical seismic profiling (w-VSP) waveform data and found that the S-wave attenuation in methane hydrate bearing sediments (MHBS) has weak frequency-dependence. Matsushima & Zhan (2020) attributed a possible S-wave attenuation mechanism to the viscous friction due to the elastic contrast between hydrate and sand grains. This viscous friction is caused by the elastic contrast between soft and hard solids and is fundamentally different from the dynamic friction. Seismic energy loss caused by grain boundary friction is important only at strains greater than approximately 10^{-6} (Winkler et al. 1979). Since these conditions are generally not encountered in exploration geophysics, dynamic frictional has not been considered important as an attenuation mechanism. It should be noted that the viscous friction due to the elastic contrast is frequency-dependent (i.e., higher frequency causes higher attenuation) while dynamic friction between two solids is not frequency-dependent. Although Matsushima and Zhan (2020) applied the same rock physics models with same input parameters as Zhan & Matsushima (2018) which investigated the frequency-dependent P-wave attenuation in the same location, the predicted S-wave attenuation curves at seismic frequencies are significantly lower than the measured value from w-VSP data. A possible reason for the underestimation of S-wave attenuation at seismic frequencies by the applied rock physics models may be due to consideration only on the frequency-dependence of the viscous friction between sand grains and hydrate and due to neglection of the dynamic friction. Therefore, by taking into account the effect of dynamic friction which is not

frequency-dependent, we may be able to explain the measured w-VSP attenuation at seismic frequencies.

There are some theories explaining the mechanisms of wave attenuation in MHBS. In terms of S-wave attenuation, the most widely approved theory is proposed by Guerin & Goldberg (2005), the base of which is Biot type three-phase theory (Biot, 1956) and was optimized by Leclaire et al. (1994) and Carcione & Tinivella (2000). This model considers squirt flow, inertial coupling, Biot flow, viscous friction, and cementation effect as the mechanisms of wave attenuation. However, the predicted attenuation according to this model cannot explain the large degree of attenuation for both sonic logging and w-VSP data observed by Matsushima & Zhan (2020).

According to the AVO (Amplitude Variation with Offset) analysis of the data obtained from a BSR (Bottom Simulating Reflector) in Florida, Ecker et al. (1998) stated that the methane hydrates do not cement with sand grains, they just contact with them. It has been recognized that the MH morphologies significantly affect the overall rock physical properties of MH-bearing sediments, and the MH morphology is dependent on the sediment lithology, pore structure, and MH saturation (Waite et al., 2009). Seismic velocity of MH-bearing sediments is known to increase compared to sediments without hydrate. The presence of MH makes the sediments stiffer, and it might cement the grains together, and then cause the bulk and shear moduli significantly increase, thus increase both P- and S-wave velocity. However, the degree of increase of velocity is dependent on hydrate saturation and hydrate morphology (Yun et al., 2005, 2007). Rock physics modeling has been applied to predict hydrate saturation using P- and S-wave velocities based on the assumption of a hydrate morphology (Chand et al., 2006; Ecker et al., 1998, 2000; Konno et al., 2015; Lee et al., 1996; Lee & Collett, 2009).

On the other hand, it has been reported that MH-bearing sediment also exhibits obvious P- and S-wave attenuation at sonic frequencies (typically 10 to 30 kHz for monopole data and 300 Hz to 8 kHz for dipole data) in several geologic environments: the Blake Ridge site (Guerin et al. 1999), the Nankai Trough (Matsushima 2005; Suzuki & Matsushima 2013), Mallik field (Guerin & Goldberg 2002; Guerin & Goldberg 2005), and the Krishna-Godavari Basin (Nittala et al. 2017) (no obvious S-wave attenuation). In contrast to high attenuation at sonic frequencies in MHBS, previous studies have indicated controversial P-wave attenuation for MHBS at seismic frequencies (typically 10 to 150 Hz) (Bellefleur et al. 2007; Matsushima 2006; Rossi et al. 2007). No significantly increased P-wave attenuation has been observed in borehole seismic data (20 to 150 Hz) (Wood et al. 2000) at VSP frequencies (30 to 110 Hz) (Matsushima 2006; Matsushima et al. 2016), at seismic frequencies (10 to 45 Hz) (Nittala et al. 2017), in ocean bottom seismograph (OBS) data (20 to 200 Hz) (Madrussani et al. 2010; Rossi et al. 2007), or from full-waveform inversion results for MHBS (8 to 24 Hz) (Jaiswal et al. 2012). In contrast, significantly increased attenuation of P-waves was observed in laboratory resonant column measurements below 550 Hz (Priest et al. 2006; Best et al. 2013), VSP data (10 to 200 Hz) (Bellefleur et al. 2007; Dvorkin & Uden 2004), and crosswell seismic data (100 to 1000 Hz) (Bauer et al. 2008). However, successful investigations on S-wave attenuation for MHBS at seismic frequencies are scarce. Priest et al. (2006) and Best et al. (2013) observed significant S-wave attenuation at frequencies below 550 Hz for synthetic MH-bearing sands using laboratory resonant column measurements.

At the Nankai Trough, P-wave attenuation in the MHBS has previously been estimated based on sonic logging data (Suzuki & Matsushima 2013) and zero-offset VSP data (Matsushima et al. 2016). The results indicated that the P-wave attenuation was frequency dependent. In order to clarify this frequency dependence of P-wave attenuation, Zhan & Matsushima (2018) performed

rock physics modeling and suggested that the effect might be due to the squirt flow caused by the combined effect of the degree of hydrate saturation and two permeable systems (namely, between sand grains and between hydrate grains) and/or due to squirt flow caused by fluid inclusions with different aspect ratios in a microporous hydrate. Matsushima & Zhan (2020) estimated S-wave intrinsic attenuation at a frequency range from 30 to 100 Hz from walkaway vertical seismic profiling (w-VSP) data. They demonstrated the significant S-wave attenuation at seismic frequencies from w-VSP data acquired in the MHBS, which implies weak frequency-dependence of S-wave attenuation in MH reservoirs through comparison with sonic logging S-wave attenuation estimates obtained by Suzuki & Matsushima (2013).

A few rock physics models have been applied to examine the effect of hydrates on the seismic attenuation of MH-bearing sediment. These models are based on either the Biot type three-phase theory or the effective medium theory. Leclaire et al. (1994) proposed a three-phase model based on the Biot theory and then incorporated Biot flow in sand grains and ice grains (hereafter called the Leclaire model). Carcione & Tinivella (2000) incorporated the interaction between hydrate and sand grains, and their subsequent cementation into the Leclaire model (hereafter called the Carcione model). Guerin & Goldberg (2005) incorporated a Biot-squirt (BISQ) attenuation mechanism proposed by Diallo & Appel (2000) into the Carcione model to take into account squirt flow in hydrate and sand grains, and further added the friction effect between hydrate and sand grains (hereafter called the Guerin model). On the other hand, Best et al. (2013) adopted the self-consistent approximation (SCA) to consider the viscous loss effect due to squirt flow caused in microporous hydrates, the viscoelastic effect of the hydrate, and Biot flow. Furthermore, Marín-Moreno et al. (2017) incorporated local viscous squirt flow between connected pores due to the formation of hydrates and gas bubble damping into this model. Zhan & Matsushima (2018) applied

the rock physics models proposed by Guerin & Goldberg (2005) and Marín-Moreno et al. (2017) to investigate the frequency-dependent P-wave attenuation at Nankai Trough. Marín-Moreno et al. (2017) indicated that their modeling results for S-wave attenuation were significantly less insensitive to the presence of hydrates than those for P-wave attenuation.

Zhan (2020) applied three types of Biot extension models (the Leclaire, Carcione, and Guerin models) to predict the S-wave attenuation. The results showed that the S-wave attenuation has multiplex dependence on the initial sand permeability, initial hydrate permeability, and MH saturation. The author averaged the sonic S-wave attenuation values calculated by Suzuki & Matsushima (2013) under each scale of MH saturation, and compared them with the predicted values. Among these predictions, the attenuation by the Leclaire model is significantly lower than those of the Carcione and Guerin models, and also than the averaged values even minus the standard deviation. As for the largest prediction case (under certain sand and hydrate permeability), the predicted values are overall 20 percentage points lower than the measured values.

In this work, we attempted to consider the dynamic friction on the contact line as the main mechanism of the S-wave attenuation. But so far, the mechanisms and the influence factor of the value of contact line friction have not been clear. There are several theories and assumptions, while none of them are widely recognized.

Waite et al. (1997) first found the energy dissipation on the three phase contact line. They made a wedge-shaped cracks, which is an open systems composed of glass slides separated by wires. They partially saturated the cracks with liquid and measured the attenuation and stiffness of the artificial sample in the extensional mode using a broad band attenuation spectrometer (l MHz–100 Hz). A non-zero, frequency independent attenuation has been measured at low frequencies in these cracks. The authors stated that for that geometry and frequency range, no viscous dissipation

is expected. Then they developed a model that explained this dissipation by a physichemical interaction that restricts the movement of the contact line. Finally, they change the sodium dodecyl sulfate (SDS) concentration and observed low frequency attenuation and crack stiffness changes. Brunner & Spetzler (2001) conducted experiments observing the dynamic miniscus (collaborative motion of contact line and contact angle) and constructed a model describing the dissipation energy on the contact line, which is only related to the drop wetting scale, contact line moving direction and surface tension of the material. The author stated that the peak value of contact angle (advancing and receding) is not related to the contact line moving velocity. Johansson & Hess (2018) conducted large-scale molecular dynamics simulations observe the microscopic mechanism of energy dissipation in contact lines. The authors state that when the contact line is moving, the inside liquid molecules moves over or displaces other liquid molecules, then the inner molecules will bounce to the outer ones, this kinetic energy transforms to thermal energy and dissipates to ouside the system. The author measured the dissipated energy and found it of the same magnitude as the dissipation in the whole bulk of the droplet. Also, the author states that the friction increases significantly as the contact angle decreases. Lindeman & Nagel (2023) conducted drop wetting and unwetting experiments and found that the changing rate of the contact angle is strongly related to the wait time (since the drop has been set on the solid) and slightly related to the flow rate of the liquid. But the underlying mechanism is totally not clear.

Understanding the dynamic behavior of fluids and accurately measuring relevant parameters in a subsurface reservoir poses significant challenges. Consequently, there is a considerable level of uncertainty associated with predicting reservoir performance. To mitigate this uncertainty, simulation studies are commonly conducted to quantify the potential variations (Aziz & Settari, 1979).Reservoir simulation involves employing a numerical model that represents the geological

and petrophysical characteristics of a hydrocarbon reservoir. This model facilitates the analysis and prediction of fluid behavior within the reservoir over a specific period (Lie & Mallison, 2015). The initial phase of constructing a reservoir model entails mathematically describing the reservoir and its petrophysical properties.In their work, Lie and Mallison (2015) introduced the concept of the Representative Element Volume (REV) as part of the mathematical description and characterization of the reservoir model (refer to Fig. 1). The REV concept is based on the notion that petrophysical flow properties remain constant within certain scales of heterogeneity. If present, REVs serve as markers that delineate transitions between different scales of heterogeneity. Moreover, they define natural length scales for modeling purposes. Rozhko (2021) constructed a rock physics model using the REV concept, which was a bulk of rock with a crack partially saturated by a drop of liquid, to explore the mechanism of the low frequency shadow appearing around the Bottom Simulating Reflector (BSR), and found that the dynamic friction on the contact line of the three phases (solid, gas and liquid) was highly underestimated. The author also conducted Fourier analysis to the strain data of the REV and observed new low frequency is generated (under bi-sinusoidal wave and Ricker wave), which appears as low-frequency shadows in seismic exploration (Taner, Koehler & Sheriff, 1979).

Low-frequency shadow is another sign of reservoir of hydrocarbon. Low-frequency shadows is defined as the phenomenon that frequency shifts to lower and amplitude increases near the bottom of a gas layer on a seismic profile. Spectral decomposition data after Fourier transformation will indicate characteristics similar to those of low-frequency shadows. Taner, Koehler & Sheriff (1979) first emphasize this phenomenon and named it “low-frequency shadow”. The authors performed complex seismic trace analysis and found a shift toward lower frequencies is often observed on reflections from reflectors below gas sands, condensate, and oil reservoirs. The author

stated that the shadows often occur only on reflections from reflectors immediately below the petroliferous zone, reflections from deeper reflectors seeming normal. This observation is empirical, and many have made the same observation, but the mechanism is not understood. Pu, Du & Xu (2021) analyzed several field data of seismic section and found that with the visual dominant seismic frequency close to 30 Hz, the peak frequency of the gas-bearing tight sandstones and tight dolomite reservoirs will move from approximately 30 to 10–15 Hz. Nearly all tight gas layers thicker than 15 m exhibit attenuation characteristics of generalized low-frequency shadows. Li & Rao (2020) constructed a impact factor model to explain the relationship between low-frequency shadows and pore-fluid properties and reservoir thickness. Low-frequency anomalies that are often observed below hydrocarbon-bearing reservoirs with time delays of approximately 100–150 ms are often referred to as low-frequency shadows according to Castagna et al. (2003), who indicate that these anomalies might be difficult to explain by simple attenuation and velocity dispersion of conventional P-waves alone. They suggest that the energy at low frequencies is amplified by some other mechanisms, an area that needs further investigation. On the other hand, Krylova & Goloshubin (2016) suggest that Krauklis waves generated at fluid-filled fractures may provide an alternative explanation for the low-frequency anomalies observed on the seismic data. Krauklis waves were first proposed and derived analytically by Krauklis (1962), and they were later simulated by numerical modeling experiments (Ferrazzini & Aki, 1987; Groenenboom & Falk, 2000; Frehner & Schmalholz, 2010) and observed in cross hole seismic measurements by Goloshubin et al (1993). According to Korneev (2015), Krauklis waves are generated by the interaction between fluids and the walls of fractures and are converted into body waves at the fracture tips. Korneev (2011), using analytical methods, concludes that the generation of low-frequency anomalies should likely be maximum in a random distribution of fractures due to the

triggering of Krauklis waves from fluid-filled fractures. Further, Ahmad et al. (2017), using target-oriented horizon-velocity analysis at the locations of low-frequency anomalies, observe low velocities associated with the low-frequency anomalies and propose that this change in velocity might be due to the generation of low-velocity, high-amplitude, low-frequency Krauklis waves.

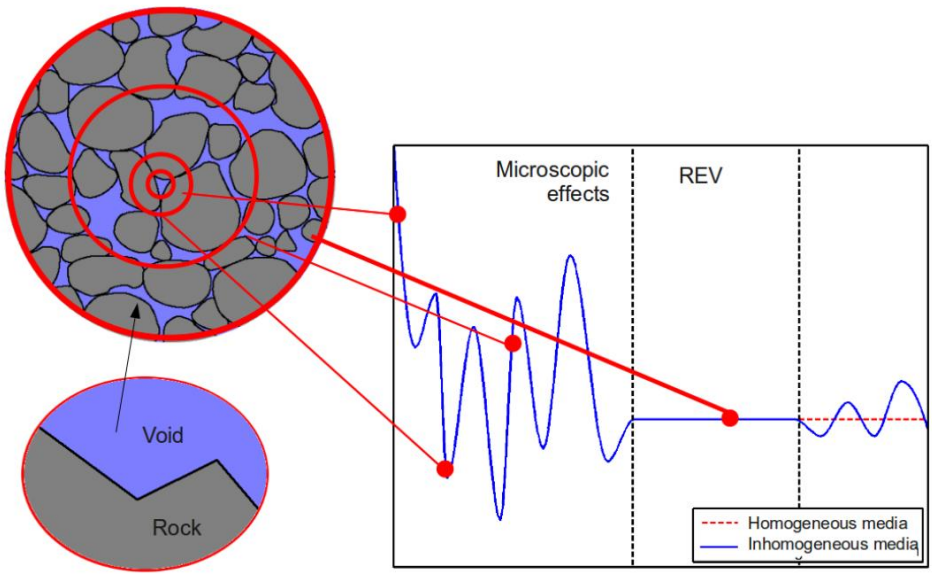

Fig. 1. Lie & Mallison (2015). *A representative elementary volume is the smallest volume over which a measurement can be made and be representative of the whole, here illustrated for porosity* [Figure]. Mathematical Models for Oil Reservoir Simulation. https://doi.org/10.1007/978-3-540-70529-1_277.

Despite numerous attempts to explain these low-frequency anomalies through numerical and physical modeling experiments, observations from real seismic data are limited. No significant attempts have been made to correlate faults and fractures with the low-frequency anomalies (to see any possible evidence of the Krauklis wave phenomenon) by using real broadband seismic data, where low frequencies are well preserved down to 4–5 Hz.

However, in S-wave seismic exploration, low-frequency shadow has never been observed. In this work, we extend the research of Rozhko (2021) to consider the case of S-wave. Rozhko first

used Muskhelishvili's theory to calculate the strain of the REV under certain stress condition, then he constructed a step system to simulate the stress change of the wave, in which by each step the stress change by a very small value, and then the condition of next step of the REV is calculated. We use the same method of Rozhko's, but the modeling part is quite different with his. In our model, the core idea continues Rozhko's paper, the consideration of dynamic friction on the contact line is considered. We predict the attenuation at broadband frequencies based on S-wave attenuation from w-VSP and sonic logging data. In order to emphasize that the viscosity dissipation has minimal impact on the attenuation, this time we regarded the methane hydrate as a kind of viscous liquid. And according to Ecker et al. (1998), the methane hydrates are mainly generating away off the connect of the grains, which cause the penetration of the MHBS to be very low, especially near the bottom simulation reflector, so there are few gases in the sediments. In this work, the three phases to form the contact are methane hydrate, sand grains and sea water.

CHAPTER 2. METHOD

Here, we developed mathematical equations for the dynamic friction on the contact line to calculate S-wave attenuation. The constructing process, assumptions, input parameters, and workflows are stated as follows.

2.1. Workflows

First, we used the same REV in Rozhko (2016). This model can consider three phase cases. In the static analysis part, we used Muskhelishvili's method (Muskhelishvili, 1977) to get the relationship between the far field stress plus the pressure of the enclosure liquid and the displacement of any point in the REV. Three cases, REV with empty, totally saturated and partially saturated crack were calculated, respectively. The first two cases were calculated to compare the results with previous research in order to validate methods. After that, we used geometric relationships in the partially saturated REV to construct the digital correlation between wave, sand and the drop. Finishing the static analysis part, cyclic stress was applied to the model, and the deformation of the REV was regarded as a quasistatic progress. This means that we ignored the wait time's effect stated by Lindeman & Nagel (2023), and also the inertia of the liquid and the sand. From one step to next step, all the one-dimensional physical quantities were taking linear continuous changes, and once the far field stress stopped change at one step, the other quantities stopped change at the step as well.

In the dynamic analysis part, a stepping system was used to describe the behavior of the contact line, because the deformation of the liquid was not linear as a result of contact line hysteresis (Rozhko, 2021). This suggests that the quantities change on both sides of one step could be nonlinear. Like one quantity stays increasing before one step but after the step it begins to drop.

This does not conflict with the linear change between steps stated in the previous paragraph. On each step, what we calculate includes the deformation of the liquid and the rock (sand), and the internal force of the REV. In this part we also conducted the calculation on the test cases. After the deformation of the REV in one cycle of the far field stress was simulated, we calculated the stored energy and dissipated energy, and finally estimated the quality factor from them.

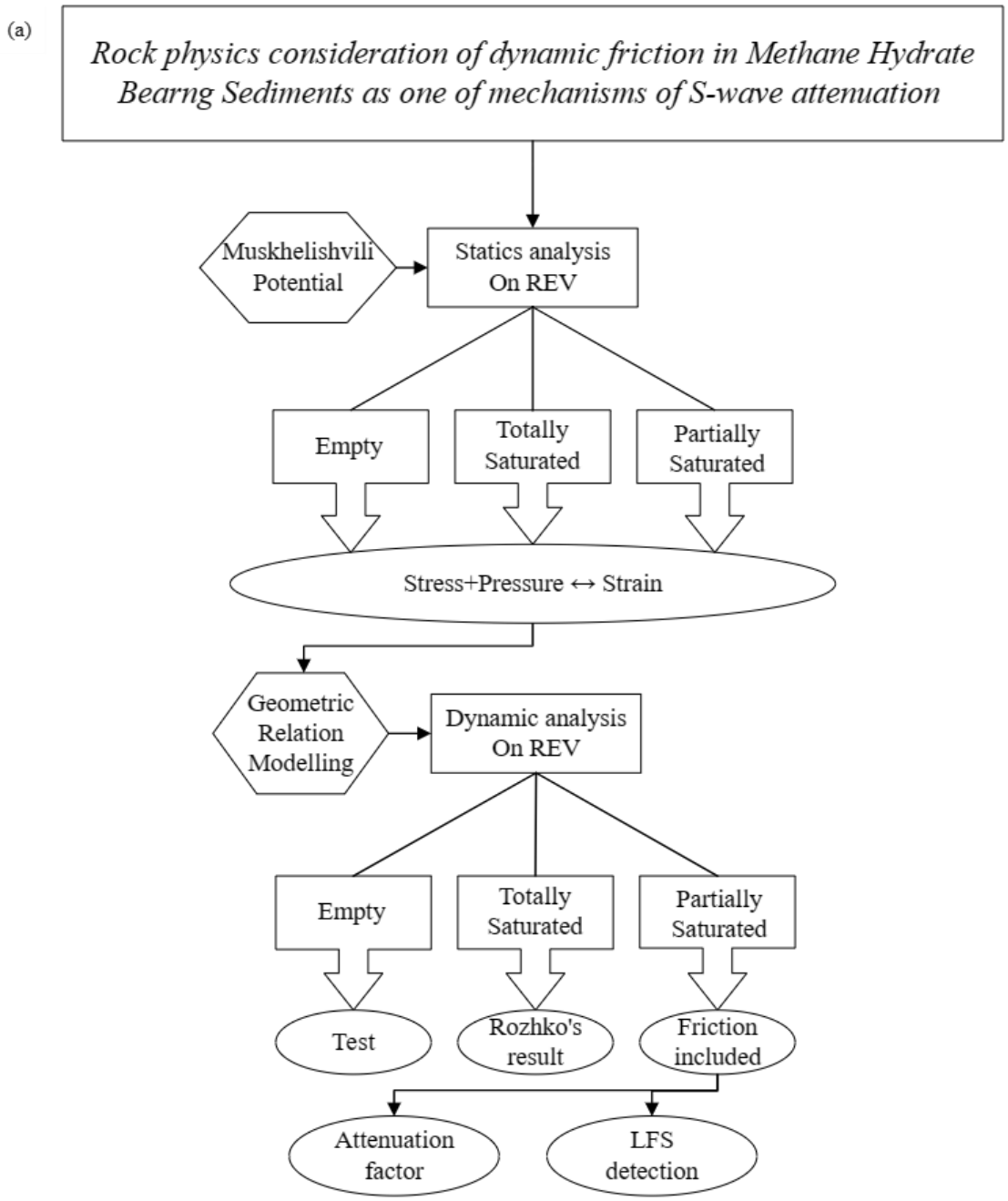

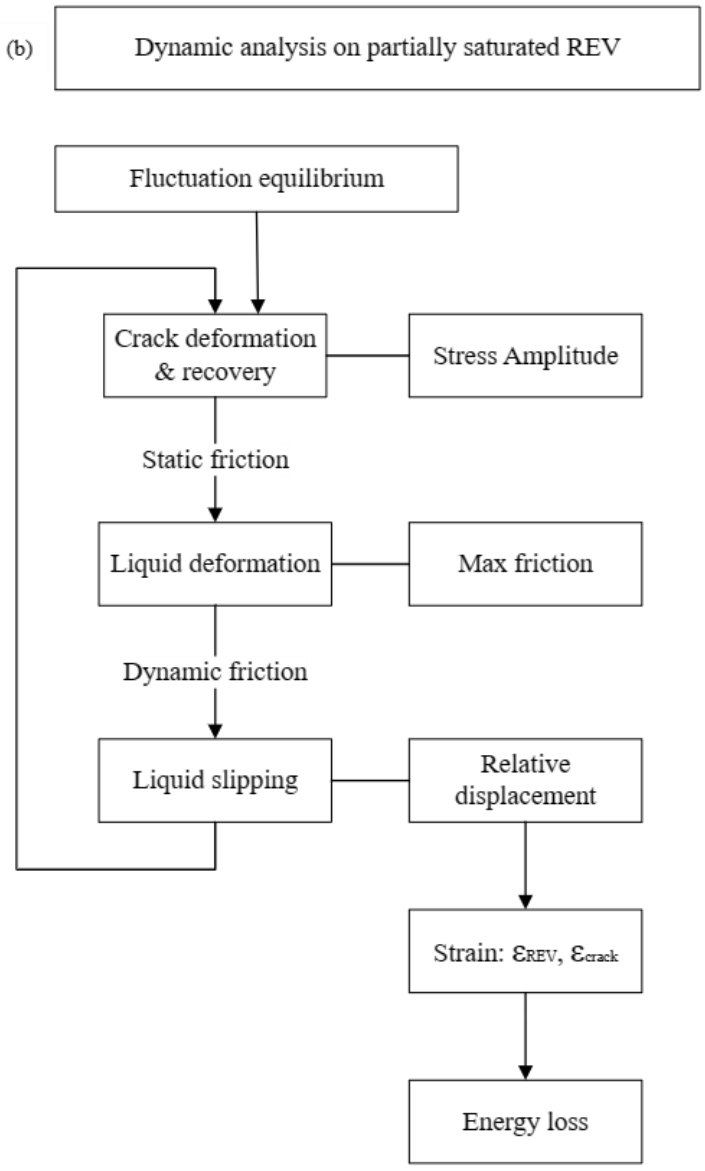

Fig. 2. (a) The overall constructing flow of the model, including method tests, verification and application. (b) Detailed flow of the dynamic analysis part.

2.2. Representative element volume (REV)

In this work, an REV is defined as a piece of rock including a crack, shown in Fig. 3(a) The crack is approximated by an elliptical cavity with the major axes of length 2*a* and minor axes of length 2*b*. In the crack, a drop of liquid is contacting the top and bottom of the crack, and the length of the wetting part is 2*c*. The *xy* section is shown in Fig. 3(b). The rock was subject to uniform

pressure P_{we} from the liquid drop on the boundary of the crack, and P_{nw} from the other parts of the boundary. In this model, the wetting part means connecting with (wetted by) methane hydrates, and the non-wetting parts were saturated by sea water. The applicability of this model is considerable because if we consider the fourth phase – gas, we can still use this REV, by just adjusting the proportion of the pore number. Anyway, in this work we do not consider gas – according to Ecker et al. (1998), the methane hydrates are mostly generated away off the connects of the sand grains, so they block the pores, which cause the permeability of MHBS to be very low. This also explains why there are plenty of suspended gas under the BSR. On the other hand, there is no significant reflector above the methane region, this means that the saturation of methane hydrate reduces as the depth decreases, which denotes that the small amount of gas escaping from under the BSR can easily get up to the sea. So, the gas saturation in the MHBS can be very low.

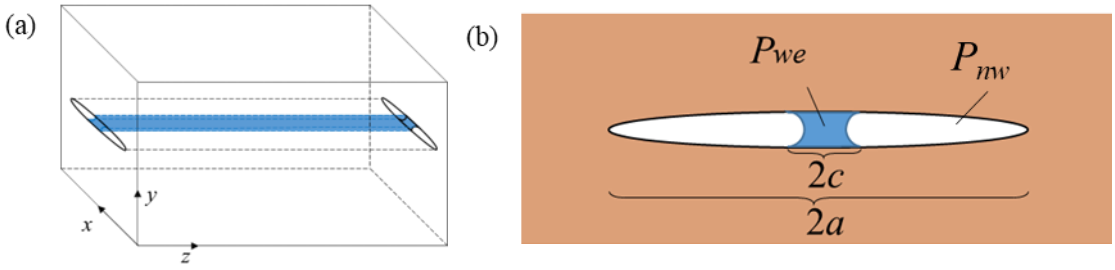

Fig. 3. (a) Representative volume element containing a partially saturated crack, approximated by an elliptical cavity of high aspect ratio, where 2*a* is major axis of ellipse. (b) The horizontal section of the model. Plane-strain approximation is used, which implies that a variation of geometry, far-field stresses and fluid pressure in z-direction is neglected. Partially saturated crack with the wetting fluid phase located symmetrically at the tips, under pressure P_{we}. The non-wetting fluid phase is located at the center, under pressure P_{nw}. The length of the interface meniscus is 2*c*.

2.3. Static analysis

In this part, only static far-field stress acts on the body. The strain of every point in the body was calculated according to Muskhelishvili (1977), in which the author offered a method with a pair of *Kolosov-Muskhelishvili potentials* that can express all the parameters including stress and

strain of the points in the body. There is no actual physical quantity corresponding to these two potentials. We can understand them as potential functions and stream functions in fluid mechanics. The definition of them is as follows. First, we define a function *U*, whose second derivative is stress, which is called Airy stress function or complex function. We all know that the Harmonic function is defined in a region of R^n and satisfies the Laplace's equation ($\Delta u = \nabla^2 u = 0$) in that region. The complex stress function has the property:

$$\frac{\partial^2 U}{\partial x^2} = \frac{\partial A}{\partial x} = \sigma_{yy} \tag{1}$$

$$\frac{\partial^2 U}{\partial y^2} = \frac{\partial B}{\partial y} = \sigma_{xx} \tag{2}$$

$$-\frac{\partial^2 U}{\partial x\, \partial y} = \frac{\partial B}{\partial x} = \frac{\partial A}{\partial y} = \sigma_{xy} \tag{3}$$

According to the equilibrium equation of elasticity (the third invariant of Cauchy strain tensor):

$$\frac{\partial \sigma_{xx}}{\partial x} + \frac{\partial \tau_{xy}}{\partial y} = 0 \tag{4}$$

$$\frac{\partial \tau_{yx}}{\partial x} + \frac{\partial \sigma_{yy}}{\partial y} = 0 \tag{5}$$

Then $\nabla^4 U = \nabla^2(\sigma_{xx} + \sigma_{yy}) = 0$, we know that *U* is a second-ordered harmonic function.

Then set $P = \nabla^2 U = \sigma_{xx} + \sigma_{yy}$, *P* is also harmonic. Set $Q = \text{conjugate}(P)$, who is also harmonic, and *P*, *Q* meet the Cauchy-Riemann condition.

Then set another analytical function $f(z) = P(x, y) + iQ(x, y)$, where $z = x + iy$. And define

$$\varphi(z) = \frac{1}{4}\int f(z)dz = p + iq \tag{6}$$

Then we can get

$$\frac{\partial p}{\partial x} = \frac{\partial q}{\partial y} = \frac{1}{4}P \tag{7}$$

$$-\frac{\partial p}{\partial y} = \frac{\partial q}{\partial x} = \frac{1}{4}Q \tag{8}$$

so p and q are conjugate and harmonic.

Then set

$$p_1 = U - px - qy \tag{9}$$

$$q_1 = \text{conjugate}(p_1) \tag{10}$$

and define

$$\chi(z) = p_1 + iq_1 \tag{11}$$

$$\psi(z) = \chi'(z) \tag{12}$$

From all the formulas above we can get

$$U = px + qy + p_1 = Re[\bar{z}\varphi(z) + \chi(z)] = \frac{1}{2}\left[\bar{z}\varphi(z) + z\overline{\varphi(z)} + \overline{\chi(z)}\right] \tag{13}$$

Combining function (1) (2) (3) and (13) we can get

$$\sigma_{xx} = \frac{1}{2}\left[2\overline{\varphi'(z)} + 2\varphi'(z) + \bar{z}\varphi''(z) + \overline{z\varphi''(z)} + \chi''(z) + \overline{\chi''(z)}\right] \tag{14}$$

$$\sigma_{yy} = \frac{1}{2}\left[2\overline{\varphi'(z)} + 2\varphi'(z) - \bar{z}\varphi''(z) - \overline{z\varphi''(z)} - \chi''(z) - \overline{\chi''(z)}\right] \tag{15}$$

$$\sigma_{xy} = \frac{i}{2}\left[\bar{z}\varphi''(z) - \overline{z\varphi''(z)} + \chi''(z) \mp \overline{\chi''(z)}\right] \tag{16}$$

We can also use these *Kolosov-Muskhelishvili potentials* to express the displacement of every point in the plane.

From the Hooke's theorem we know that:

$$E\varepsilon_{xx} = \sigma_{xx} - \upsilon\sigma_{yy} \tag{17}$$

$$E\varepsilon_{yy} = \sigma_{yy} - \upsilon\sigma_{xx} \tag{18}$$

$$\varepsilon_{xy} = \frac{\sigma_{xy}}{2\mu} \tag{19}$$

where E is Young's modulus, υ is Poisson's ratio and μ is the shear modulus. Then the relationships between strain and displacement:

$$\varepsilon_{xx} = \frac{\partial u_x}{\partial x} \tag{20}$$

$$\varepsilon_{yy} = \frac{\partial u_y}{\partial y} \tag{21}$$

$$\varepsilon_{xy} = \frac{1}{2}\left(\frac{\partial u_y}{\partial x} + \frac{\partial u_x}{\partial y}\right) \tag{22}$$

Combining formula (14) (15) (16) with (17) (18) (19) and (20) (21) (22) we can get:

$$E\frac{\partial u_x}{\partial x} = 2\left[\varphi'(z) + \overline{\varphi'(z)}\right]$$
$$-(1+\upsilon)\frac{1}{2}\left[2\overline{\varphi'(z)} + 2\varphi'(z) - \bar{z}\varphi''(z) - \overline{z\varphi''(z)} - \chi''(z) - \overline{\chi''(z)}\right] \tag{23}$$

$$E\frac{\partial u_y}{\partial y} = 2\left[\varphi'(z) + \overline{\varphi'(z)}\right]$$
$$-(1+\upsilon)\frac{1}{2}\left[2\overline{\varphi'(z)} + 2\varphi'(z) + \bar{z}\varphi''(z) + \overline{z\varphi''(z)} + \chi''(z) + \overline{\chi''(z)}\right] \quad (24)$$

Integrate the two formulas above and we can get:

$$u_x = \frac{2}{E}\left[\varphi(z) + \overline{\varphi(z)}\right]$$
$$-\frac{1+\upsilon}{2E}\left[\varphi(z) + \overline{\varphi(z)} + \bar{z}\varphi'(z) + \overline{z\varphi'(z)} + \chi'(z) + \overline{\chi'(z)}\right] \quad (25)$$

$$u_y = \frac{2}{E}\left[\varphi(z) + \overline{\varphi(z)}\right]$$
$$-\frac{1+\upsilon}{2E}\left[\varphi(z) - \overline{\varphi(z)} - \bar{z}\varphi'(z) + \overline{z\varphi'(z)} - \chi'(z) + \overline{\chi'(z)}\right] \quad (26)$$

Then the displacement of each point in the REV can be expressed.

But here comes the question that a set of certain far field stress cannot determine a unique group of φ and ψ (see the case below).

First, we provide the far field stress group σ_{xx}, σ_{yy} and σ_{xy} (also τ_{xy}). We get

$$\sigma_{xx} + \sigma_{yy} = 4Re[\varphi'(z) + Ci] \quad (27)$$

$$\sigma_{yy} - \sigma_{xx} + 2i\tau_{xy} = 2[\bar{z}\varphi''(z) + \psi'(z)] \quad (28)$$

where C is an arbitrary real constant. Then we can get

$$\varphi(z) = \int \varphi'(z) + Ciz + \gamma \quad (29)$$

$$\psi(z) = \int \psi'(z) + \gamma' \quad (30)$$

where γ and γ' are arbitrary complex constant, so we set the boundary conditions:

$$\varphi(0) = 0 \tag{31}$$

$$\mathrm{Im}[\varphi'(0)] = 0 \tag{32}$$

$$\psi(0) = 0 \tag{33}$$

For the stress from inside the crack, we calculate it by the followings. First, we set the resultant force function:

$$F(x,y) = \frac{\partial U}{\partial x} + i\frac{\partial U}{\partial y} = \varphi(z) + \overline{z\varphi'(z)} + \psi'(z) \tag{34}$$

Then for an arbitrary arc AB on the boundary of the crack, the consultant force can be expressed as:

$$X + iY = \int_{AB} (x_n + iY_n)ds = i\left[\frac{\partial U}{\partial x} + i\frac{\partial U}{\partial y}\right]_A^B = -i\left[\varphi(z) + \overline{z\varphi'(z)} + \psi'(z)\right]_A^B \tag{35}$$

Combine the formula (34) and (35):

$$F(x,y) = i(X + iY) + \text{const.} \tag{36}$$

Then the author put out a result that

$$\varphi(z) = -\frac{X + iY}{2\pi(1+\varkappa)}\log z + \Gamma z + \varphi_0(z) \tag{37}$$

$$\psi(z) = -\frac{\varkappa(X + iY)}{2\pi(1+\varkappa)}\log z + \Gamma' z + \psi_0(z) \tag{38}$$

where

$$\Gamma = \frac{1}{4}(\sigma_{xx} + \sigma_{yy}) \tag{39}$$

$$\Gamma' = \frac{1}{2}\left(\sigma_{yy} - \sigma_{xx} + 2i\tau_{xy}\right) \tag{40}$$

and $\varphi_0(z)$ and $\psi_0(z)$ are determined by the boundary condition (31) (32) and (33), and are determined by the condition of the certain case, the calculation of which is shown in the following text.

Because the whole element has uniformity along *z* axis, so only the parameters in the section plane is to be calculated. A mapping function is used to transform the plain with an elliptical hole (a multiply connected region) into a circular plain, a simply connected region (shown in Fig. 4). Then the *Kolosov-Muskhelishvili potentials* can be expressed as holomorphic functions. Associated with Cauchy integral theory, the displacement (strain) on each coordinate can be calculated.

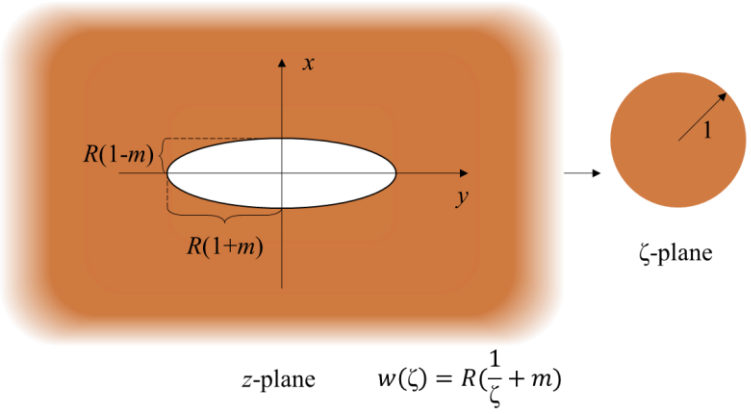

Fig. 4. Mapping function *w* transforms the section plane into a circular region.

The used parameters in this calculation are listed in Table 1. Some of the related symbols and the relations are simply stated in the table.

Table 1. Used and some of the related symbols in the Muskhelishvili's method.

Symbol	Meaning
X, *Y*, *Z*	Stress components
N	Principle stress
λ, μ	$\lambda = \frac{E\sigma}{(1+\upsilon)((1-2\upsilon))}, \mu = \frac{E}{2(1+\upsilon)}$

E	Young's modulus
υ	Poisson's ratio
$\varkappa$	$=\frac{\lambda+3\mu}{\lambda+\mu}$
u, v, w	Displacement components on x, y, z
U	Stress function $U(x,y)$, the second derivative is stress
P, Q	$P = \nabla^2 \mathrm{U} = X_x + Y_y$, Q = conjugate of P, $\frac{\partial P}{\partial x} = \frac{\partial Q}{\partial y}$, $\frac{\partial P}{\partial y} = -\frac{\partial Q}{\partial x}$
f(z)	Resultant force from inside the crack. $f(z) = P+iQ$
φ	*Muskhelishvili potential* 1. $\varphi(z) = p + iq$, every biharmonic function of p, q can be expressed by function of z = $x + iy$
$\chi(z)$	Function of z to let $px + qy + p1 = U = \varkappa[\bar{z}\varphi(z) + \chi(z)]$ $\bar{z}$: conjugate of z
ψ	= dχ / dz, *Muskhelishvili potential* 1
Γ	$Real(\Gamma) = B = \frac{1}{4}(N_1+N_2), \Gamma' = B' + iC' = -\frac{1}{2}(N_1-N_2)e^{-2i\alpha}$ N_1, N_2 are the principal stress at infinity.
$\varphi_1, \psi_1, \Phi_1, \Psi_1$ ()	New expression of φ…
ρ, ϑ	Polar radius and angle of the curvilinear coordinates
σ	$e^{i\vartheta}$, an arbitrary point on the unit circle
ζ	$\rho e^{i\vartheta}$a point in REV
r	The circle | ζ |=1
ω()	A map from ζ to z, $z = \omega(\zeta) = c/\zeta +$ a holomorphic function
R	$\frac{a+b}{2}$(semi-major / minor axis) (auxiliary)
m	$\frac{a-b}{a+b}$(auxiliary)

In this case, the far field stress and the liquid pressure are shown in Fig. 5. For the far field stress, X_x and Y_y are both 0, and shear stress is equal to τ. z_1, z_2, z_3 and z_4 are the coordinates of the contact lines in Cartesian coordinate system. Then we can get:

$$\Gamma = 0\,,\ \Gamma' = i\tau \tag{41}$$

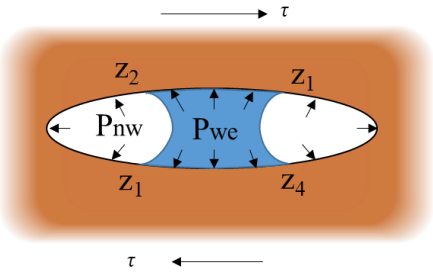

Fig. 5. The stress situation of the REV in the case of the present study.

The variation of the resultant f around the boundary of the crack are $-P_{we}dz$ and $-P_{nw}dz$ in wetting and non-wetting parts respectively.

Then the increasement of f is

$$Incf = -P_{we}[z_2 - z_1 + z_4 - z_3] + P_{nw}[z_3 - z_2 + z_1 - z_4] \tag{42}$$

Then, $X + iY = i\ Incf\ ,\ X - iY = i\ \overline{Incf}$. And we can get the f_0 term in the residual terms φ_0 and ψ_0 of *Muskhelishvili potentials* φ and ψ:

$$f_0 = f - \frac{X + iY}{2\pi i}\log\sigma + \frac{X - iY}{2\pi i(1+\varkappa)} \cdot \frac{\sigma^2 + m}{1 - m\sigma^2} \tag{43}$$

Then φ_0 and ψ_0 can be derived by the following progress:

$$\varphi_0 = 2\pi i \left\{ \begin{array}{l} \int_{\sigma_2}^{\sigma_1} P_{we}\left(\sigma - \frac{m}{\sigma}\right)\frac{d\sigma}{\sigma - \zeta} + \int_{\sigma_2}^{\sigma_3}\left[P_{we}z_2 + P_{nw}R\left(\sigma - \frac{m}{\sigma}\right)\right]\frac{d\sigma}{\sigma - \zeta} \\ + \int_{\sigma_3}^{\sigma_4}\left[P_{we}z_2 + P_{nw}(z_3 - z_2) + P_{we}R\left(\sigma - \frac{m}{\sigma}\right)\right]\frac{d\sigma}{\sigma - \zeta} \\ + \int_{\sigma_4}^{\sigma_1}\left[P_{we}z_2 + P_{nw}(z_3 - z_2) + P_{we}(z_4 - z_3) + P_{nw}R\left(\sigma - \frac{m}{\sigma}\right)\right]\frac{d\sigma}{\sigma - \zeta} \end{array} \right\}$$
$$- \frac{Incf}{2\pi}\frac{1}{2\pi i}\int_{\gamma}\frac{\log\sigma}{\sigma - \zeta}d\sigma - \frac{\overline{Incf}}{2\pi(1+\varkappa)} \cdot \frac{1}{2\pi i}\int_{\gamma}\frac{\sigma^2 + m}{1 - m\sigma^2}\frac{d\sigma}{\sigma - \zeta} \tag{44}$$

$$\psi_0 = \frac{1}{2\pi i}\int_{\gamma}\frac{\overline{f_0}d\,\sigma}{\sigma - \zeta} - \zeta\frac{1 + m\zeta^2}{\zeta^2 - m}\varphi_0'(\zeta) \tag{45}$$

We substituted these results into the function of *Muskhelishvili potentials* φ and ψ, refer to the APPENDIX for specific results.

$$\varphi(\zeta) = \Gamma R\zeta - \frac{X + iY}{2\pi(1+\varkappa)}\log\zeta + \varphi_0 \tag{46}$$

$$\psi(\zeta) = \Gamma' R\zeta - \frac{\varkappa(X - iY)}{2\pi(1+\varkappa)}\log\zeta + \psi_0 \tag{47}$$

where R and m are from the shape of the crack (Fig. 4), $\Gamma, \Gamma', P_{we}, P_{nw}$, are derived from the stress situation, $\varkappa$ is from the property of the rock(Table 1), and z_1 to z_4 and σ_1 to σ_4 are determined by

the saturation situation of the liquid. All parameters are known from the experiment conditions. The last remaining variable ζ represents the curvilinear coordinate of the point.

Finally, the displacement function of every point in the REV can be calculated by the following formula:

$$2\mu|\omega'(\zeta)| \cdot \left(\upsilon_\rho + i\upsilon_\vartheta\right) = \frac{\bar{\zeta}}{\rho}\overline{\omega'(\zeta)}\left(\varkappa\varphi(\zeta) - \frac{\omega(\zeta)}{\overline{\omega'(\zeta)}}\overline{\varphi'(\zeta)} - \overline{\psi(\zeta)}\right) \tag{48}$$

Here we did a test on the applicability of this method, the input parameters are shown in the Table 2. To highlight the influence of the liquid pressure, we set the P_{we} to be much higher than P_{nw}, and the illustration of the deformation of the crack is shown in the Fig. 6.

Here because the difference of the P_{we} and the P_{nw} is too huge, fore single points appear on the contact line. Yet, the displacement is still very small, the order of magnitude of which is 10^{-7}.

Table 2. Input parameters of the test case of Muskhelishvili's method.

Parameters	value
Young's modulus (E) (GPa)	30
Poisson's ratio (υ)	0.3
semi-major axis (a) (m)	10^{-3}
semi-minor axis (b) (m)	10^{-6}
ϑ_1 (rad)	1.155
ϑ_2 (rad)	1.987
ϑ_3 (rad)	4.297
ϑ_4 (rad)	5.128
P_{we} (Pa)	10^5
P_{nw} (Pa)	0
σ_x (Pa)	0
σ_y (Pa)	0
τ (Pa)	10^7

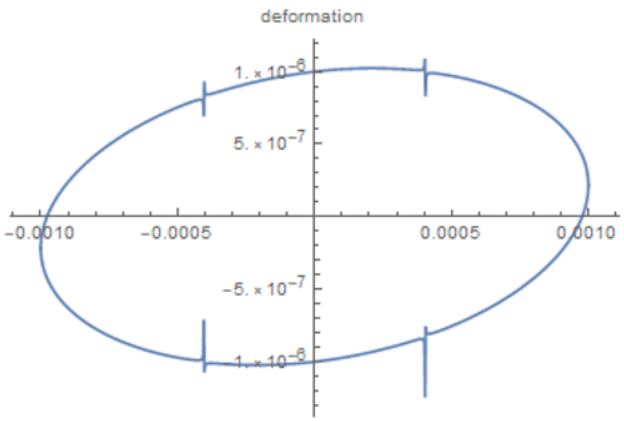

Fig. 6. Illustration of the deformation of the crack in the test case of Muskhelishvili's method.

In the input parameters, the ϑ_1 to ϑ_4 are the polar angle of the coordinates of the four contact lines. For the calculation convenience, we set the four contact lines lie on the symmetric locations on the undeformed crack boundary.

Finally, we can extract the vertical displacement of the midpoint of the crack boundary, whose θ coordinate is $\frac{\pi}{2}$ and ρ is equal to 1 for it is on the boundary of the crack, which we name it $n_o(\tau)$ for convenience in dynamic analysis. Having done these, we can apply the wave stress on the unit volume of the sediment to start the dynamic analysis.

2.4. Dynamic analysis

When the shear wave propagates through the REV, the crack begins to deform, and the liquid drop will follow so, which will cause the contact angle to get larger on one side and smaller on the other side (shown in Fig. 7). It is because there is dynamic friction on the contact lines that they do not move once there is deformation.

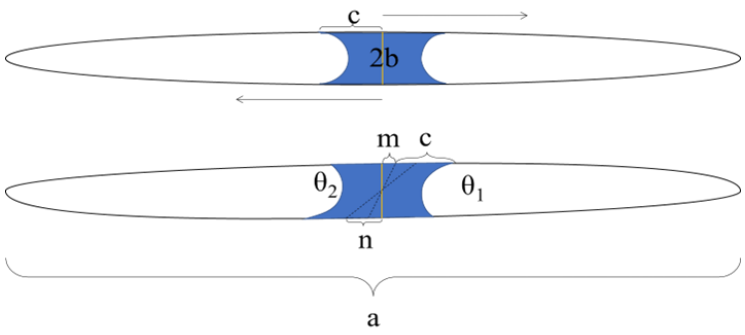

Fig. 7. The draft of deformation of the crack and the liquid drop. The *m* is the displacement of the midpoint of the liquid drop, the *n* is that of the crack, and *c* is the half width of the hydrate drop.

In this process of the contact line moving and not moving, the friction leads to the dissipation and storage of elastic potential energy. The draft of the displacement of the midpoint of the crack and the hydrate trop under triangular stress is shown in Fig. 8.

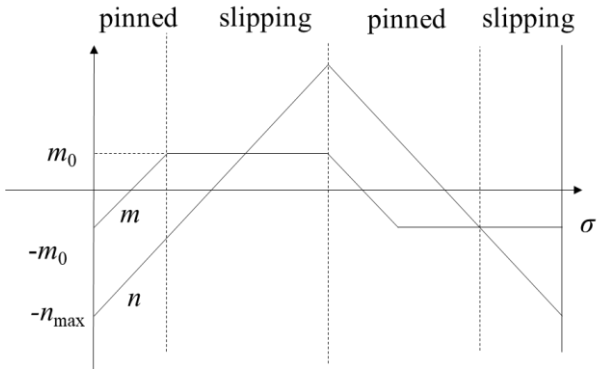

Fig. 8. Displacement under triangular stress, where *m* is the displacement of the midpoint of the hydrate drop, and *n* is that of the crack.

The n_{max} is derived in the static analysis, and m_0 can also be calculated by geometric relationship. When the *n* gets to the n_{max}, the meniscus of the hydrate drop will conform to Fig. 9. And the m_0 can be calculated by the following formulas:

$$2m_0 \cdot tan\frac{\pi + \theta_a - \theta_r}{2} = h_P \tag{49}$$

Where

$$h_p = b\sqrt{1 - \frac{(c - n_{max} + m_0)^2}{a^2}} \tag{50}$$

Once the parameters in Table 2 are determined, the m_0 is an unchanged value. We change the saturation of the methane hydrate (who determines the coordinates of the contact lines) in the pore and get the m_0 and $n_{\max}$ under the saturation of from 0.1 to 0.9.

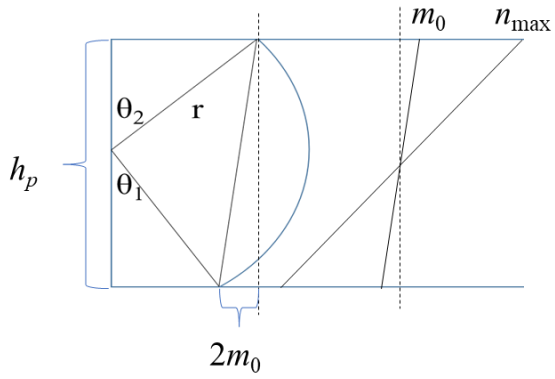

Fig. 9. The geometric relationship between displacement and contact angle. At this moment, θ_2 is equal to θ_a, and θ_1 is equal to θ_r.

Next, the θ_2 and θ_1 can be expressed by m:

$$\theta_1 = \frac{\theta_a + \theta_r}{2} - m \cdot \frac{\theta_a - \theta_r}{2m_0} (m \in [0, m_0]) \tag{51}$$

$$\theta_2 = \frac{\theta_a + \theta_r}{2} + m \cdot \frac{\theta_a - \theta_r}{2m_0} (m \in [0, m_0]) \tag{52}$$

The dynamic friction on the contact line and the viscous friction can be also calculated by the following equations:

$$f_d = 4(\gamma_{ML} * \cos\theta_1 + \gamma_{MS} - \gamma_{LS}) \tag{53}$$

$$f_v = \frac{\eta m A v}{d} \tag{54}$$

where γ_{ML}, γ_{MS} and γ_{LS} are the surface tensions between methane hydrate, liquid and sand. η is the viscosity of the methane hydrate. *A* is the area of the contact surface and *v* is the relative velocity of the upper and lower layers, and *d* is the distance of them. Then the deformation of the crack n under new stress condition can be expressed as $n_o(\tau - f_d - f_v)$. Then we started the step simulation. The initial value of *m* was 0. Every step we calculate the variation of *n*, *dn* and made a judgement: if this step's *m* plus *dn* exceeds the range [$-m_0$,m_0], *m* stays the original value; if not, *m* returns *m*+*dn*. And the relative velocity of the two layers can also be calculated by *dn*/step size. The value of $\gamma_{ML}, \gamma_{MS}, \gamma_{LS}, \eta$ and other input parameters are shown in the next part.

After the simulation of one cycle of the wave, the attenuation is calculated by the following steps. The strain of the crack is defined as

$$\varepsilon_{cr} = \frac{n}{a} \tag{55}$$

Then according to Betti's reciprocal theory (Walsh, 1965), the strain of the REV can be defined as

$$\varepsilon_{REV} = \frac{\Delta\tau}{G} \cdot (1 - porosity) + \varepsilon_{cr} \cdot porosity \tag{56}$$

where *G* is the shear modulus of the enclosing sand. The porosity denotes the real value of the methane hydrate bearing sediments. Next, the undrained shear modulus of the REV is expressed as:

$$G_{REV} = \frac{\Delta\tau}{\varepsilon_{REV}} \tag{57}$$

In this formula, the wave strain and wave stress are chosen from the peak value in one cycle for the energy calculation.

Then the wave energy is divided into two parts, the elastic energy and dissipated energy. The elastic part is calculated by the following formula:

$$W_{REV} = \frac{\Delta\tau^2}{2G_{REV}} \tag{58}$$

and the dissipated part in one cycle is calculated as:

$$\Delta W_{REV} = \oint \Delta\tau \mathrm{d}\varepsilon_{REV} \tag{59}$$

Finally, the attenuation factor can be calculated as follows:

$$\frac{1}{Q_{REV}} = \frac{\Delta W_{REV}}{2\pi \cdot W_{REV}} \tag{60}$$

The simulated result of the displacement of the midpoint of hydrate drop and crack boundary is shown in Fig. 10.

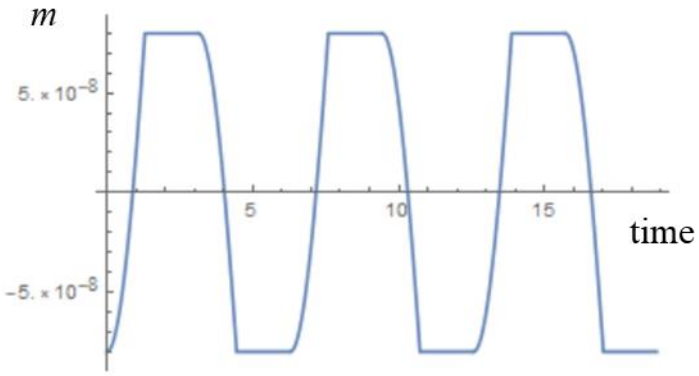

Fig. 10. The displacement of the hydrate drop midpoint.

2.5. Spectrum analysis

In Rozhko (2021), P-wave is applied to the REV and low-frequency shadows are detected under bi-sinusoidal waveform and Licker waveform. In this work, the same operation is applied to the shear bi-sinusoidal case.

Bi-sinusoidal waveform is defined as

$$y = A_1 \sin(\omega_1 x + \varphi_1) + A_2 \sin(\omega_2 x + \varphi_2),$$

in which $\omega_1 \neq \omega_2$.

After we finished the dynamic analysis, we let the stress wave continue to act for tens of cycles, get the data of the midpoint displacement of the crack boundary under multiple cycles, and carried out Fourier analysis on it.

Fig. 11 shows the multiple-cycled data of displacement of hydrate drop and the crack boundary for the Fourier analysis. The figure shows the data in the time domain of 0-4s, and the analyzed data has the step size of 10^{-4} second and simulation duration of 5 seconds.

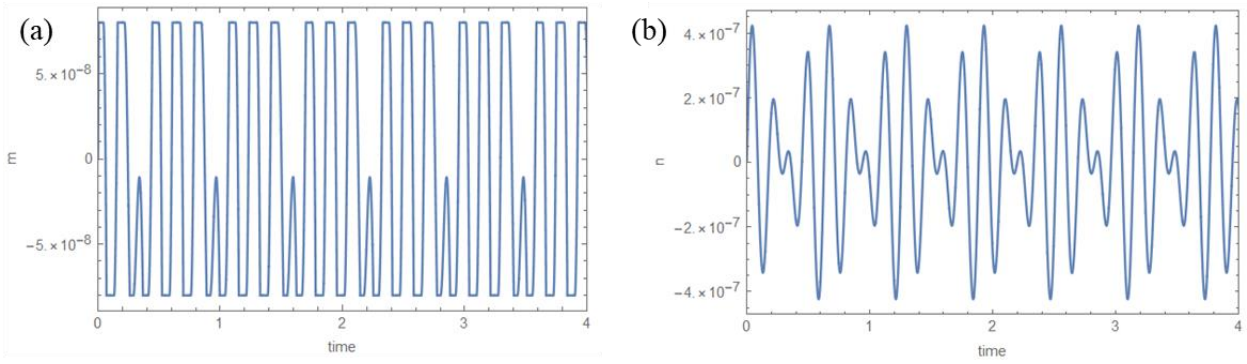

Fig. 11. Multiple cycles of the hydrate drop displacement (a) and crack boundary midpoint displacement (b).

Finally, we put the frequency spectrums of the crack boundary displacement and the stress of the wave. If there is new lower frequency than the inherent frequency of the wave in the displacement spectrum, then it means we have the low frequency shadows. But this is obviously not the result we want, because according to situ data, S-wave in MHBS does not show low-frequency shadows.

2.6. Input parameters

(a) Young's modulus and the poison ratio of sand in the enclosing sand:

According to the logging data of MITI Nankai Trough wells, the methane hydrate mainly distributed in the depth of 165~327 meters under the sea floor, which belongs to Kakegawa stratum group. The skeleton of sediments is mainly composed of dark gray mudstone or siltstone and light gray fine- to medium-grained sands (Takashi et al., 2004). And the methane hydrate is mainly found in the sands. In the mudstone or siltstone, the saturation of methane hydrate is very low. It is almost impossible to measure the physical properties of MHBS, since the pressure and temperature requirement is so limited for the preservation of MHBS.

Miyazaki et al. (2011) conducted several triaxial compression experiments on different kinds of MHBS specimens, Toyoura sand, number 7 silica sand and number 8 silica sand and got the data of Young's modulus and Poisson ratio under different MH saturation. In this work, the model only needs the properties of the skeleton, so the ones under zero saturation are to be referred to. Young's modulus and Poisson ratio are determined to be 300 MPa and 0.3, respectively.

(b) Porosity and MH saturation:

From the log data in MITI Nankai Trough in 1999 and 2000, the methane hydrate dominant layers usually have the porosity of 42%~46% and the methane hydrate saturation of up to50%~90% (Takashi et al., 2004; Akihisa et al., 2002).

(c) Pore size:

Uchida & Tsuji (2004) used Mercury porosimetry method to measure the pore size distribution. The mean pore radius occurred on around 200 nm in most depth of the MHBS from 160~315 meters under the sea floor.

(d) Saturation of a certain pore:

According to the AVO analysis (Ecker et al., 1998) of the data obtained from a BSR in Florida, the methane hydrates dose not cement with sand grains, they just contact with them. Also, because the hydrates are off the contacts of the sand grains, so they block the pores, which cause the permeability of MHBS to be very low. This also explains why there are plenty of suspended gas under the BSR. On the other hand, there is no significant reflector above the methane region, this means that the saturation of methane hydrate reduces as the depth decreases, which denotes that the small amount of gas escaping from under the BSR can easily get up to the sea. So, the gas saturation in the MHBS can be very low.

On the other hand, according to Waite et al. (2009), the proportion of the contact morphology start to appear at the total saturation of around 40% and grows with it. in this work the proportion of the contact morphology pores is assumed to be {0.05, 0.06, 0.07, 0.08, 0.3, 0.4, 0.5, 0.6, 0.9} at the total hydrate saturation of 0.1 to 0.9.

(e) Contact angle, surface tension and viscosity of methane hydrate:

The quantification of the contact line friction is still not clear so far. Although the mechanism of it has been successfully simulated by Johansson & Hess (2018), but the behavior of the contact line is still influenced by many factors in some unknown ways. In this work we refer to Rozhko (2016) and introduce a pair of constant advancing and receding contact angle. When the contact angle is between these two values, the contact line is pinned on the solid, and when it gets to one of the two values and tend to exceed one, the contact line would start to slip (Adam & Jessop, 1925). Fig. 12 shows the approximate contact line behavior and the change of the contact angle. In this theory, the contact angle is a manifestation of the surface tension and the roughness of the solid.

In this model, the methane hydrate is assumed as viscous liquid. But we lack laboratory data about the contact angle surface tension and viscosity. The value of the advancing and receding contact angles are related to the roughness of the solid, the surface tension of the liquids, and the pressure (Zhao, 2019). Here we referred to the parameters of Rozhko (2021), and also attempted to choose another lager range for the experiment. For the viscosity, though the molecular weight and intermolecular force components of water and methane hydrate are very similar, we assume it as a much larger value than that of water. Dispite this, the viscous dissipation is still insignificant, which furter proved that the viscous friction does not dominate the attenuation in methane hydrate bear sediments (Matsushima & Zhan, 2020).

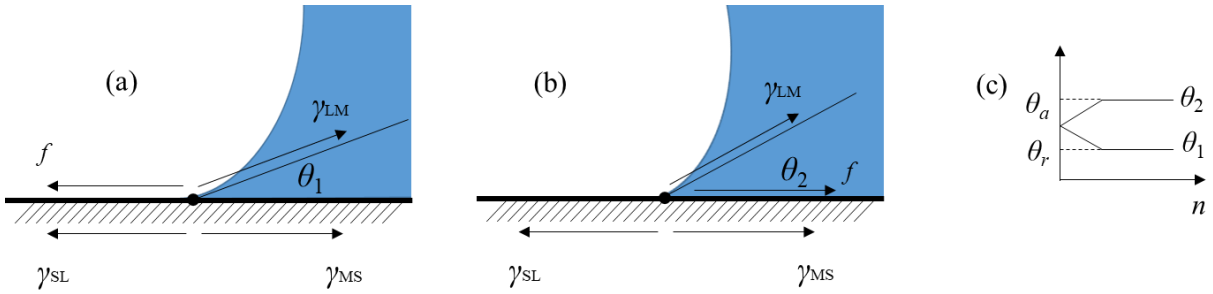

Fig. 12. (a) The relationship between the friction f and the surface tensions γ_{LV}, γ_{SV} and γ_{SL} when the contact line is receding. (b) Advancing case. Where S, L, and V mean solid, liquid and vapor. (c) The value change of θ_1 and θ_2. When m gets to m_0, θ_1 and θ_2 stop to change.

The exact input parameters in the model are listed in Table 3.

Table 3. Input parameters in the concact line friction model.

	Case 1	Case 2	Case 3
Young's modulus (E) (MPa)	300	300	300
Poisson's ratio (v)	0.3	0.3	0.3
Surface tension (γ) (Pa · m)	0.072	0.072	0.072
Advancing contact angle (θ_a) (°)	30	60	30
Receding contact angle (θ_r) (°)	25	20	25
Effective stress (τ) (MPa)	10	10	10
Major semiaxis (a) (m)	3×10^{-7}	3×10^{-7}	3×10^{-7}
Minor semiaxis (b) (m)	2×10^{-7}	2×10^{-7}	2×10^{-7}
Porosity (n_{cr}) (%)	43	43	43
Viscosity of water (η_w) (Pa·s)	1.1×10^{-3}	1.1×10^{-3}	1.1×10^{-3}

Viscosity of methane hydrate(η_m) (Pa·s)	0.5	0.5	0.5
Frequency of sinusoidal wave (rad/s)	40	40	400

But in the spectrum analysis part, the purpose was to detect the existence of low-frequency shadow, so the input parameters were the same as Rozhko (2021).

CHAPTER 3. RESULTS

Fig. 13 shows the S-wave attenuation predicted by our contact line friction model. The saturation range starts from 10% because when it is 0 there will be errors in the calculation of m_0. The results indicate that the attenuation is strongly dependent on the range of contact angle (Case 1 and Case 2), because this range determines the duration of work done by contact line friction. Under the contact line ranging from 25°~30°, the attenuation predicted fits well with the measured data. Under different frequency of the wave (Case 1 and Case 3), the attenuation has low difference, which also matches the low difference between the actual data from w-VSP and sonic attenuation. The S-wave attenuation is predicted better than that of using optimized Leclaire, Carcione, and Guerin models calculated by Zhan (2020).

Fig. 14 shows the Fourier spectrum of crack boundary displacement and the stress of the wave. No new low frequency is generated in the displacement data like the situation in Rozhko (2021). This result also conforms to the situ results in S-wave case. In this aspect the contact line friction model is proved reasonable.

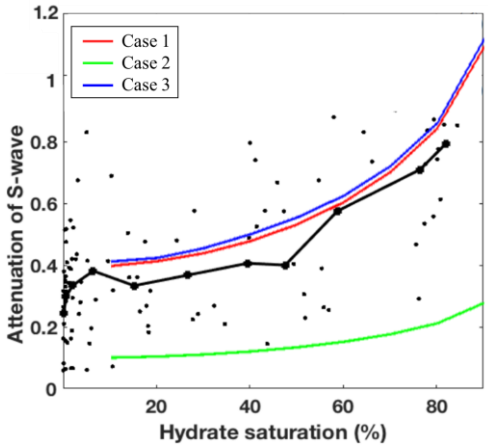

Fig. 13. Measured S-wave attenuation (black lines) and predicted attenuation by contact line friction model (colored lines) of difference cases: Case 1 (wave frequency – 40 rad/s, contact angle – 25°~30°), Case 2 (wave

frequency – 40 rad/s, contact angle – 20°~60°) and Case 3 (wave frequency – 400 rad/s, contact angle – 25°~30°).

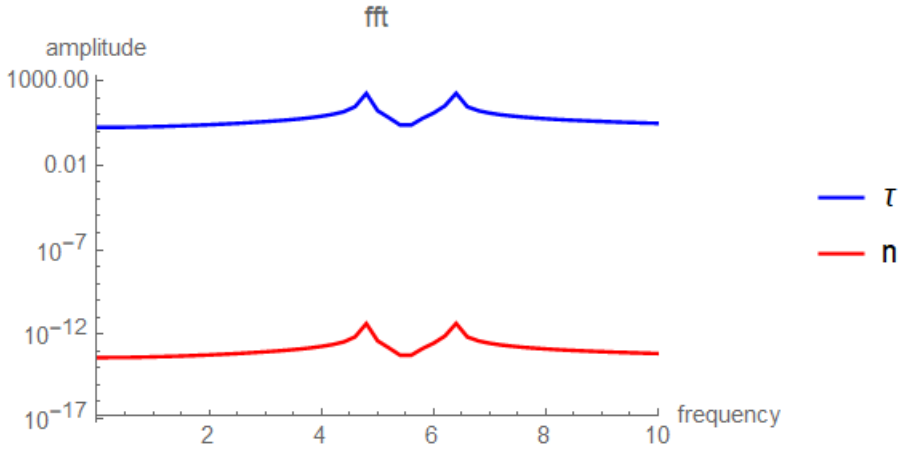

Fig. 14. Fourier spectrum of the crack boundary displacement (n) and the stress of the wave (τ).

CHAPTER 4. DISCUSSION

The primary objective of this study was to investigate the factors contributing to S-wave attenuation and develop a comprehensive model to simulate energy dissipation. In a study conducted by Zhan (2020), three different Biot extension models (Leclaire, Carcione, and Guerin) were employed to predict S-wave attenuation in MHBS (Methane Hydrate-Bearing Sediments). However, all three models significantly underestimated the measured values obtained from w-VSP (wireline Vertical Seismic Profiling) data.

It is postulated that the frequency-dependence of friction between sand grains and hydrate may be a plausible explanation for this underestimation. Specifically, at sonic frequencies, the dominant mechanism for S-wave attenuation is attributed to the friction occurring between sand and hydrate grains. This friction, caused by the elastic contrast, displays frequency-dependent characteristics, meaning that higher frequencies result in increased attenuation. It is important to note that dynamic friction between solid materials does not exhibit frequency dependence.To address this discrepancy and comprehend the measured attenuation at seismic frequencies, the present study incorporates the effect of dynamic friction on the contact line as one of the mechanisms influencing S-wave attenuation.

In the contact line friction model, the squirt flow is not considered because we regarded that S-wave would not cause volume change of the pores, as a result, the pressure change of the liquid and hydrate in a certain pore is approaching to zero.

The real situation of MHBS is based on pore space among sand grains. In this model we assumed that a crack corresponds to a pore space. The boundaries of the crack are the surfaces of the sand grains, and the spikes of the crack are the connect of the sand grains. Another approach assumes that a pore space consists of several cracks.

Theoretically, the attenuation by the contact line friction model under 0 hydrate saturation should be around 0 (only viscous dissipation), which conflicts with the measured data. We speculate that there are some gas bubbles in the low hydrate saturation areas, because in these areas, the permeability of the sediments is much higher than high saturation areas. By simulation, the contact line friction between the three phases of water, gas and sand also causes considerable energy dissipation. This might be the reason why there is still attenuation around 0.3 in the 0 hydrate areas.

The contact line friction model regards the methane hydrate as a kind of viscous liquid. For the exact property of it under the condition of deep seabed, we still need more laboratory data support. Another conjecture is that methane hydrate exhibits solid properties when it rubs against rocks, which can also be verified through simulation experiments. Both the ideas base on the AVO analysis done by Ecker et al. stating that there is no cementing morphology in the MHBS. If this is proved wrong by coring or artificial synthesis experiment, the contact line model should be optimized to consider the cementing morphology by incorporating a new proportion that increasing the Young's modulus of sand.

CHAPTER 5. CONCLUSIONS

The present study demonstrated the significant S-wave attenuation at seismic frequencies from w-VSP data acquired in the MHBS, which implies weak frequency-dependence of S-wave attenuation in MH reservoirs. By construct a model considering the dynamic friction on the contact line and compare the prediction with the w-VSP data in situ area, we infer that the friction between hydrate and sand grains is a reasonable mechanism of the S-wave attenuation. And we also draw the conclusion that the dynamic friction dominates the S-wave attenuation much more than viscous friction for the small difference between different frequencies. Finally, the effect of dynamic friction which is not frequency-dependent may explain the weak frequency-dependence of S-wave attenuation between sonic logging and seismic frequencies.

ACKNOWLEDGEMENTS

I would like to express my sincere gratitude to all those who have supported me throughout the completion of this research project.

First and foremost, I am deeply grateful to my advisor, Jun MATSUSHIMA and Masaatsu AICHI, for their guidance, patience, and invaluable insights. Their expertise and unwavering support have been instrumental in shaping this work and my growth as a researcher.

I would also like to extend my appreciation to the faculty members of the Matsushima's Lab for their encouragement, stimulating discussions, and constructive feedback during the course of my studies. Their commitment to excellence has inspired me to strive for academic rigor and intellectual curiosity.

I am indebted to my friends and family who have provided me with unwavering encouragement and understanding throughout this journey. Their love, support, and motivation have been invaluable sources of strength.

In conclusion, I am profoundly grateful to all those who have contributed directly or indirectly to the realization of this research project. Your assistance and encouragement have been truly invaluable.

APPENDIX

$$\phi = \Gamma_1 \zeta R + \frac{1}{2\pi} i \left(\frac{R P_{nw} \left(\zeta \left(e^{i\theta_2} - e^{i\theta_3} \right) + \left(\zeta^2 + m \right) \left(\log\left(-\zeta + e^{i\theta_2} \right) - \log\left(-\zeta + e^{i\theta_3} \right) \right) - i (\theta_2 - \theta_3) m \right)}{\zeta} + \frac{R P_{nw} \left(\zeta \left(e^{i\theta_4} - e^{i\theta_1} \right) - \left(\zeta^2 + m \right) \left(\log\left(-\zeta + e^{i\theta_1} \right) - \log\left(-\zeta + e^{i\theta_4} \right) \right) + i (\theta_1 - \theta_4) m \right)}{\zeta} + \frac{R P_{we} \left(\zeta \left(e^{i\theta_1} - e^{i\theta_2} \right) + \left(\zeta^2 + m \right) \left(\log\left(-\zeta + e^{i\theta_1} \right) - \log\left(-\zeta + e^{i\theta_2} \right) \right) - i (\theta_1 - \theta_2) m \right)}{\zeta} + \frac{R P_{we} \left(\zeta \left(e^{i\theta_3} - e^{i\theta_4} \right) + \left(\zeta^2 + m \right) \left(\log\left(-\zeta + e^{i\theta_3} \right) - \log\left(-\zeta + e^{i\theta_4} \right) \right) - i (\theta_3 - \theta_4) m \right)}{\zeta} \right)$$

$$\psi = \Gamma_2 R \zeta - \frac{i \zeta \left(m \zeta^2 + 1 \right)}{2\pi \left(\zeta^2 - m \right)} \left(\frac{P_{we} R \left(\left(\frac{1}{e^{i\theta_2} - \zeta} - \frac{1}{e^{i\theta_1} - \zeta} \right) \left(\zeta^2 + m \right) + e^{i\theta_1} - e^{i\theta_2} + 2\zeta \left(\log\left(e^{i\theta_1} - \zeta \right) - \log\left(e^{i\theta_2} - \zeta \right) \right) \right)}{\zeta} + \frac{P_{nw} R \left(\left(\frac{1}{e^{i\theta_3} - \zeta} - \frac{1}{e^{i\theta_2} - \zeta} \right) \left(\zeta^2 + m \right) + e^{i\theta_2} - e^{i\theta_3} + 2\zeta \left(\log\left(e^{i\theta_2} - \zeta \right) - \log\left(e^{i\theta_3} - \zeta \right) \right) \right)}{\zeta} + \frac{P_{nw} R \left(\left(\frac{1}{e^{i\theta_1} - \zeta} - \frac{1}{e^{i\theta_4} - \zeta} \right) \left(\zeta^2 + m \right) - e^{i\theta_1} + e^{i\theta_4} - 2\zeta \left(\log\left(e^{i\theta_1} - \zeta \right) - \log\left(e^{i\theta_4} - \zeta \right) \right) \right)}{\zeta} + \frac{P_{we} R \left(\left(\frac{1}{e^{i\theta_4} - \zeta} - \frac{1}{e^{i\theta_3} - \zeta} \right) \left(\zeta^2 + m \right) + e^{i\theta_3} - e^{i\theta_4} + 2\zeta \left(\log\left(e^{i\theta_3} - \zeta \right) - \log\left(e^{i\theta_4} - \zeta \right) \right) \right)}{\zeta} - \frac{P_{we} R \left(\left(e^{i\theta_1} - e^{i\theta_2} \right) \zeta + \left(\zeta^2 + m \right) \left(\log\left(e^{i\theta_1} - \zeta \right) - \log\left(e^{i\theta_2} - \zeta \right) \right) - i m (\theta_1 - \theta_2) \right)}{\zeta^2} - \frac{P_{nw} R \left(\left(e^{i\theta_2} - e^{i\theta_3} \right) \zeta + \left(\zeta^2 + m \right) \left(\log\left(e^{i\theta_2} - \zeta \right) - \log\left(e^{i\theta_3} - \zeta \right) \right) - i m (\theta_2 - \theta_3) \right)}{\zeta^2} - \frac{P_{nw} R \left(\left(-e^{i\theta_1} + e^{i\theta_4} \right) \zeta - \left(\zeta^2 + m \right) \left(\log\left(e^{i\theta_1} - \zeta \right) - \log\left(e^{i\theta_4} - \zeta \right) \right) + i m (\theta_1 - \theta_4) \right)}{\zeta^2} - \frac{P_{we} R \left(\left(e^{i\theta_3} - e^{i\theta_4} \right) \zeta + \left(\zeta^2 + m \right) \left(\log\left(e^{i\theta_3} - \zeta \right) - \log\left(e^{i\theta_4} - \zeta \right) \right) - i m (\theta_3 - \theta_4) \right)}{\zeta^2} \right) +$$

$$\frac{i}{2\pi}$$

$$\left(-\frac{1}{2\bar{\zeta}^3}P_{we}\,R\left(e^{2i\theta_1}\,m\,\bar{\zeta}^2-e^{2i\theta_2}\,m\,\bar{\zeta}^2+2\log\left(1-e^{i\theta_1}\,\bar{\zeta}\right)\bar{\zeta}^2-2\log\left(1-e^{i\theta_2}\,\bar{\zeta}\right)\bar{\zeta}^2+2\,e^{i\theta_1}\,m\,\bar{\zeta}-\right.\right.$$

$$2\,e^{i\theta_2}\,m\,\bar{\zeta}+2\,m\log\left(1-e^{i\theta_1}\,\bar{\zeta}\right)-2\,m\log\left(1-e^{i\theta_2}\,\bar{\zeta}\right)\Big)-\frac{1}{2\bar{\zeta}^3}$$

$$P_{nw}\,R\left(e^{2i\theta_2}\,m\,\bar{\zeta}^2-e^{2i\theta_3}\,m\,\bar{\zeta}^2+2\log\left(1-e^{i\theta_2}\,\bar{\zeta}\right)\bar{\zeta}^2-2\log\left(1-e^{i\theta_3}\,\bar{\zeta}\right)\bar{\zeta}^2+2\,e^{i\theta_2}\,m\,\bar{\zeta}-\right.$$

$$2\,e^{i\theta_3}\,m\,\bar{\zeta}+2\,m\log\left(1-e^{i\theta_2}\,\bar{\zeta}\right)-2\,m\log\left(1-e^{i\theta_3}\,\bar{\zeta}\right)\Big)-\frac{1}{2\bar{\zeta}^3}$$

$$P_{we}\,R\left(e^{2i\theta_3}\,m\,\bar{\zeta}^2-e^{2i\theta_4}\,m\,\bar{\zeta}^2+2\log\left(1-e^{i\theta_3}\,\bar{\zeta}\right)\bar{\zeta}^2-2\log\left(1-e^{i\theta_4}\,\bar{\zeta}\right)\bar{\zeta}^2+2\,e^{i\theta_3}\,m\,\bar{\zeta}-\right.$$

$$2\,e^{i\theta_4}\,m\,\bar{\zeta}+2\,m\log\left(1-e^{i\theta_3}\,\bar{\zeta}\right)-2\,m\log\left(1-e^{i\theta_4}\,\bar{\zeta}\right)\Big)+\frac{1}{2\bar{\zeta}^3}$$

$$P_{nw}\,R\left(e^{2i\theta_1}\,m\,\bar{\zeta}^2-e^{2i\theta_4}\,m\,\bar{\zeta}^2+2\log\left(1-e^{i\theta_1}\,\bar{\zeta}\right)\bar{\zeta}^2-2\log\left(1-e^{i\theta_4}\,\bar{\zeta}\right)\bar{\zeta}^2+2\,e^{i\theta_1}\,m\,\bar{\zeta}-\right.$$

$$\left.\left.2\,e^{i\theta_4}\,m\,\bar{\zeta}+2\,m\log\left(1-e^{i\theta_1}\,\bar{\zeta}\right)-2\,m\log\left(1-e^{i\theta_4}\,\bar{\zeta}\right)\Big)\right)\right.$$

REFERENCES

Adam, N.K. & Jessop, G. (1925). CCL.—Angles of contact and polarity of solid surfaces. J. Chem. Soc., Trans., 127(0), pp.1863–1868. doi:https://doi.org/10.1039/ct9252701863.

Ahmad, S.S., Brown, R.J., Escalona, A. & Rosland, B.O. (2017). Frequency-dependent velocity analysis and offset-dependent low-frequency amplitude anomalies from hydrocarbon-bearing reservoirs in the southern North Sea, Norwegian sector. GEOPHYSICS, 82(6), pp.N51–N60. doi:https://doi.org/10.1190/geo2016-0555.1.

Akihisa, B.K., Tezuka, K., Senoh, O. & Uchida, T. (2002). Well Log Evaluation Of Gas Hydrate Saturation In The Miti Nankai-Trough Well, Offshore South East Japan. [online] onepetro.org. Available at: https://onepetro.org/SPWLAALS/proceedings/SPWLA-2002/All-SPWLA-2002/SPWLA-2002-BB/27245 [Accessed 28 May 2023].

Aziz K. & Settari A. (1979). Petroleum Reservoir Simulation. Applied Science Publishers, [online] 476. Available at: https://cir.nii.ac.jp/crid/1573950398841360000 [Accessed 18 Jul. 2023].

Bauer, K., Pratt, R. G., Haberland, C., & Weber, M. (2008). Neural network analysis of crosshole tomographic images: The seismic signature of gas hydrate bearing sediments in the Mackenzie Delta (NW Canada). *Geophysical Research Letters*, *35*, L19306. doi:10.1029/2008GL035263

Boswell, R., & Collett, T. S. (2011). Current perspectives on gas hydrate resources. Energy Environ. Sci., 4(4), 1206–1215. https://doi.org/10.1039/C0EE00203H

Brunner, W. & Spetzler, H.A. (2001). Observations of time-dependent meniscus behavior with implications for seismic attenuation in three-phase systems. Geophysical Research Letters, 28(9), pp.1867–1870. doi:https://doi.org/10.1029/2000gl012173.

Bellefleur, G., Riedel, M., Brent, T., Wright, F., & Dallimore, S. R. (2007). Implication of seismic attenuation for gas hydrate resource characterization, Mallik, Mackenzie Delta, Canada. *Journal of Geophysical Research: Solid Earth*, *112*, B10311. doi:10.1029/2007JB004976

Best, A. I., Priest, J. A., Clayton, C. R. I., & Rees, E. V. L. (2013). The effect of methane hydrate morphology and water saturation on seismic wave attenuation in sand under shallow sub-seafloor conditions. *Earth and Planetary Science Letters*, *368*, 78–87. doi:10.1016/j.epsl.2013.02.033

Carcione, J. M., & Tinivella, U. (2000). Bottom-simulating reflectors: Seismic velocities and AVO effects. *Geophysics*, *65*(1), 54–67. Retrieved from http://dx.doi.org/10.1190/1.1444725

Castagna, J.P., Sun, S. & Siegfried, R.W. (2003). Instantaneous spectral analysis: Detection of low-frequency shadows associated with hydrocarbons. The Leading Edge, 22(2), pp.120–127. doi:https://doi.org/10.1190/1.1559038.

Chand, S., Minshull, T. A., Gei, D., & Carcione, J. M. (2004). Elastic velocity models for gas-hydrate-bearing sediments—a comparison. *Geophysical Journal International*, *159*(2), 573–590. doi:10.1111/j.1365-246X.2004.02387.x

Chand, S., Minshull, T. A., Priest, J. A., Best, A. I., Clayton, C. R. I., & Waite, W. F. (2006). An effective medium inversion algorithm for gas hydrate quantification and its application to laboratory and borehole measurements of gas hydrate-bearing sediments. *Geophysical Journal International*, *166*(2), 543–552. doi:10.1111/j.1365-246X.2006.03038.x

Charles K. Paull, W. P. D. (2001). Natural gas hydrates: occurrence, distribution, and detection. (W. P. Dillon & C. K. Paull, Eds.). Washington, DC: American Geophysical Union. Retrieved from http://onlinelibrary.wiley.com/book/10.1029/GM124

Dawe, R. A., & Thomas, S. (2007). A large potential methane source - Natural gas hydrates. Energy Sources, Part A: Recovery, Utilization and Environmental Effects, 29(3), 217–229. https://doi.org/10.1080/009083190948676

Diallo, M. S., & Appel, E. (2000). Acoustic wave propagation in saturated porous media: Reformulation of the Biot/Squirt flow theory. *Journal of Applied Geophysics*, *44*(4), 313–325. doi:10.1016/S0926-9851(00)00009-4

Ecker, C., Dvorkin, J., & Nur, A. (1998). Sediments with gas hydrates: Internal structure from seismic AVO. *Geophysics*, *63*(5), 1659. doi:10.1190/1.1444462

Ecker, C., Dvorkin, J., & Nur, A. M. (2000). Estimating the amount of gas hydrate and free gas from marine seismic data. *Geophysics*, *65*(2), 565–573. doi:10.1190/1.1444752

Ferrazzini, V. & Aki, K. (1987). Slow waves trapped in a fluid-filled infinite crack: Implication for volcanic tremor. Journal of Geophysical Research, 92(B9), p.9215. doi:https://doi.org/10.1029/jb092ib09p09215.

Frehner, M. & Schmalholz, S.M. (2010). Finite-element simulations of Stoneley guided-wave reflection and scattering at the tips of fluid-filled fractures. 75(2), pp.T23–T36. doi:https://doi.org/10.1190/1.3340361.

Gennady Goloshubin, Krauklis, P.V., Molotkov, L.A. & Helle, H.B. (1993). Slow wave phenomena at seismic frequencies. doi:https://doi.org/10.1190/1.1822623.

Goupillaud, P. L. (1961). An approach to inverse filtering of near surface effects from seismic records. *Geophysics*, 26, 754– 760.

Groenenboom, J. & Falk, J. (2000). Scattering by hydraulic fractures: Finite-difference modeling and laboratory data. 65(2), pp.612–622. doi:https://doi.org/10.1190/1.1444757.

Guerin, G., & Goldberg, D. (2002). Sonic waveform attenuation in gas hydrate-bearing sediments from the Mallik 2L-38 research well, Mackenzie Delta, Canada. *Journal of Geophysical Research B: Solid Earth*, *107*, B5. doi:10.1029/2001JB000556

Guerin, G., & Goldberg, D. (2005). Modeling of acoustic wave dissipation in gas hydrate-bearing sediments. *Geochemistry, Geophysics, Geosystems*, *6*, Q07010. doi:10.1029/2005GC000918

Guerin, G., Goldberg, D., & Meltser, A. (1999). Characterization of in situ elastic properties of gas hydrate-bearing sediments on the Blake Ridge. *Journal of Geophysical Research*, *104*(B8), 781–795. doi:10.1029/1999JB900127

Haq, B. U. (1999). Methane in the deep blue sea. Science, 285(5427), 543–544. https://doi.org/10.1126/science.285.5427.543

Huang, J. W., Bellefleur, G., & Milkereit, B. (2009). Seismic modeling of multidimensional heterogeneity scales of mallik gas hydrate reservoirs, Northwest territories of Canada. *Journal of Geophysical Research: Solid Earth*, 114(B7) , B07306. http://doi.org/10.1029/2008JB006172

H. Schütt, Johann Michael Köhler, Boyd, O. & Hartmut Spetzler (2000). Seismic Attenuation in Partially Saturated Dime-shaped Cracks. 157(3), pp.435–448. doi:https://doi.org/10.1007/s000240050007.

Jaiswal, P., Dewangan, P., Ramprasad, T., & Zelt, C. A. (2012). Seismic characterization of hydrates in faulted, fine-grained sediments of Krishna-Godavari Basin: Full waveform inversion. *Journal of Geophysical Research: Solid Earth*, *117*, B10305 doi:10.1029/2012JB009201

Jin, Y., Konno, Y., Yoneda, J., Kida, M., & Nagao, J. (2016). In situ methane hydrate morphology investigation: natural gas hydrate-bearing sediment recovered from the eastern Nankai Trough area. *Energy and Fuels*, *30*(7), 5547–5554. doi:10.1021/acs.energyfuels.6b00762

Johansson, P. & Hess, B. (2018). Molecular origin of contact line friction in dynamic wetting. Physical Review Fluids, 3(7). doi:https://doi.org/10.1103/physrevfluids.3.074201.

Kelland, M. (1994). Natural gas hydrates: Energy for the future. Marine Pollution Bulletin, 29(6–12), 307–311. https://doi.org/10.1016/0025-326X(94)90645-9

Kvenvolden, K. A. (1993). Gas hydrates—geological perspective and global change. Reviews of Geophysics, 31(2), 173–187. https://doi.org/10.1029/93RG00268

Korneev, V.A. (2011). Krauklis wave in a stack of alternating fluid-elastic layers. GEOPHYSICS, 76(6), pp.N47–N53. doi:https://doi.org/10.1190/geo2011-0086.1.

Konno, Y., Jin, Y., Yoneda, J., Kida, M., Egawa, K., Ito, T., et al. (2015). Effect of methane hydrate morphology on compressional wave velocity of sandy sediments : Analysis of pressure cores obtained in the Eastern Nankai Trough. *Marine and Petroleum Geology*, *66*, 425–433. doi:10.1016/j.marpetgeo.2015.02.021

Krauklis, P.V. (1962). On some low-frequency vibrations of a liquid layer in an elastic medium. 26(6), pp.1685–1692. doi:https://doi.org/10.1016/0021-8928(62)90203-4.

Krylova, A. & Goloshubin, G. (2017). A seismic reflection from isotropic-fractured fluid-saturated layer. Geophysical Prospecting, 65, pp.59–67. doi:https://doi.org/10.1111/1365-2478.12510.

Leclaire, P., Cohen-Ténoudji, F., & Aguirre-Puente, J. (1994). Extension of Biot's theory of wave propagation to frozen porous media. *The Journal of the Acoustical Society of America*, *96*(6), 3753–3768. doi:10.1121/1.411336

Lee, M. W., & Collett, T. S. (2009). Gas hydrate saturations estimated from fractured reservoir at Site NGHP-01-10, Krishna-Godavari Basin, India. *Journal of Geophysical Research: Solid Earth*, *114*, B07102. doi:10.1029/2008JB006237

Lee, M.W., & Waite F.W. (2007). Amplitude loss of sonic waveform due to source coupling to the medium. *Geophysical Research Letters*, 34, L05303, doi: 10.1029/2006GL029015.

Lee, M. W., Hutchinson, D. R., Collett, T. S., & Dillon, W. P. (1996). Seismic velocities for hydrate-bearing sediments using weighted equation. *Journal of Geophysical Research: Solid Earth*, *101*(B9), 20347–20358. doi:10.1029/96JB01886

Lie, K.-A. and Mallison, B.T. (2015). Mathematical Models for Oil Reservoir Simulation. pp.850–856. doi:https://doi.org/10.1007/978-3-540-70529-1_277.

Lindeman, C. & Nagel, S.R. (2023). State-and-rate friction in contact-line dynamics. 107(6). doi:https://doi.org/10.1103/physreve.107.065111.

Li, S. & Rao, Y. (2020). Poroelastic property analysis of seismic low-frequency shadows associated with gas reservoirs. 17(3), pp.463–474. doi:https://doi.org/10.1093/jge/gxaa005.

Madrussani, G., Rossi, G., & Camerlenghi, A. (2010). Gas hydrates, free gas distribution and fault pattern on the west Svalbard continental margin. *Geophysical Journal International*, *180*(2), 666–684. doi:10.1111/j.1365-246X.2009.04425.x

Marín-Moreno, H., Sahoo, S. K., & Best, A. I. (2017). Theoretical modeling insights into elastic wave attenuation mechanisms in marine sediments with pore-filling methane hydrate. *Journal of Geophysical Research: Solid Earth*, *122*(3), 1835–1847. doi:10.1002/2016JB013577

Marketos, G., & Best, A. I. (2010). Application of the BISQ model to clay squirt flow in reservoir sandstones. *Journal of Geophysical Research: Solid Earth*, *115*, B06209. doi:10.1029/2009JB006495

Maslin, M., Owen, M., Betts, R., Day, S., Dunkley Jones, T., & Ridgwell, A. (2010). Gas hydrates: past and future geohazard? Philosophical Transactions. Series A, Mathematical,

Physical, and Engineering Sciences, 368(1919), 2369–2393. https://doi.org/10.1098/rsta.2010.0065

Matsushima, J. (2005). Attenuation measurements from sonic waveform logs in methane hydrate-bearing sediments at the Nankai Trough exploratory well off Tokai, central Japan. *Geophysical Research Letters*, *32*, L03306. doi:10.1029/2004GL021786

Matsushima, J. (2006). Seismic wave attenuation in methane hydrate-bearing sediments vertical seismic profiling data from the Nankai trough exploratory well, offshore Tokai, central Japan. *Journal of Geophysical Research: Solid Earth, 111*, B10101. doi:10.1029/2005JB004031

Matsushima, J. (2007). Seismic attenuation from VSP data in methane hydrate-bearing sediments. *Exploration Geophysics*, 38(1), 29-36.

Matsushima, J., Ali, M. Y., & Bouchaala, F. (2016). Seismic attenuation estimation from zero-offset VSP data using seismic interferometry. *Geophysical Journal International*, *204*(2), 1288–1307. doi:10.1093/gji/ggv522

Matsushima, J. & Zhan, L. (2020). S-wave attenuation estimation from walkaway vertical seismic profiling data in methane hydrate-bearing sediments at Nankai Trough, Japan. Journal of Applied Geophysics, 173, p.103931. doi:https://doi.org/10.1016/j.jappgeo.2019.103931.

McIver, R. D. (1977). Hydrates of Natural Gas--Important Agent in Geologic Processes. Geological Society of America-Abstracts with Programs, 20(9), 1089–1090. Retrieved from http://archives.datapages.com/data/HGS/vol20/no09/03.htm

Miyazaki, K., Masui, A., Sakamoto, Y., Aoki, K., Tenma, N. & Yamaguchi, T. (2011). Triaxial compressive properties of artificial methane hydrate bearing sediment. Journal of Geophysical Research, 116(B6). doi:https://doi.org/10.1029/2010jb008049.

N.I. Muskhelishvili, Some Basic Problems in the Mathematical Theory of the Elasticity, Springer, Berlin (1977)

National Program for Oil and Gas Prospecting. (1999). HY Exploratory Drilling and Resource Assessment Project "Nankai Trough"

Nittala, S., Sain, K., & Nara, D. (2017). Seismic vis-a-vis sonic attenuation in gas hydrate bearing sediments of Krishna-Godavari basin, Eastern Margin of India. *Geophysical Journal International*, *209*(2), 1195–1203. doi:10.1093/gji/ggx089

Paull, C. K., Brewer, P. G., Ussler, W., Peltzer, E. T., Rehder, G., & Clague, D. (2002). An experiment demonstrating that marine slumping is a mechanism to transfer methane from seafloor gas-hydrate deposits into the upper ocean and atmosphere. Geo-Marine Letters, 22(4), 198–203. https://doi.org/10.1007/s00367-002-0113-y

Paull, C. K., Ussler, W., Dallimore, S. R., Blasco, S. M., Lorenson, T. D., Melling, H., et al. (2007). Origin of pingo-like features on the Beaufort Sea shelf and their possible relationship to decomposing methane gas hydrates. Geophysical Research Letters, 34(1), 1–5. https://doi.org/10.1029/2006GL027977

Priest, J. A., Best, A. I., & Clayton, C. R. I. (2006). Attenuation of seismic waves in methane gas hydrate-bearing sand. *Geophysical Journal International*, *164*(1), 149–159. doi:10.1111/j.1365-246X.2005.02831.x

Pu, R., Du, X. & Xu, P. (2021). Cases of generalized low-frequency shadows of tight gas reservoirs. 9(4), pp.B39–B50. doi:https://doi.org/10.1190/int-2020-0243.1.

Quan, Y., & Harris, J. M. (1997). Seismic attenuation tomography using the frequency shift method. *Geophysics*, *62*(3), 895. doi:10.1190/1.1444197

Rossi, G., Gei, D., Böhm, G., Madrussani, G., & Carcione, J. (2007). Attenuation tomography: an application to gas-hydrate and free gas detection. *Geophysical Prospecting*, *55*(5), 655–669.

Rozhko, A.Y. (2016). Two-phase fluid-flow modeling in a dilatant crack-like pathway. Journal of Petroleum Science and Engineering, [online] 146, pp.1158–1172. doi:https://doi.org/10.1016/j.petrol.2016.08.018.

Rozhko, A.Y. (2021). On the spectral changes of seismic wave energy by a partially saturated crack due to the hysteresis of liquid bridges phenomenon. 86(3), pp.MR133–MR147. doi:https://doi.org/10.1190/geo2020-0685.1.

Ruppel, C. D., & Kessler, J. D. (2017). The interaction of climate change and methane hydrates. Reviews of Geophysics, 55(1), 126–168. https://doi.org/10.1002/2016RG000534

Sloan E.D. and Koh C.A. (2007). Clathrate Hydrates of Natural Gases. [online] Google Books. CRC Press. Available at: https://books.google.co.jp/books?hl=zh-CN&lr=&id=T7LC8ldaVR4C&oi=fnd&pg=PP1&dq=Sloan [Accessed 17 Jul. 2023].

Stoll, R. D., & Bryan, G. M. (1970). Wave Attenuation in Saturated Sediments. *The Journal of the Acoustical Society of America*, *47*(5), 1440–1447. doi:10.1121/1.1912054

Suzuki, H., & Matsushima, J. (2013). Quantifying uncertainties in attenuation estimation at methane-hydrate-bearing zones using sonic waveform logs. *Geophysics*, *78*(5), D339–D353. doi:10.1190/GEO2012-0495.1

Taner, M.T., Koehler, F. & Sheriff, R.E. (1979). Complex seismic trace analysis. GEOPHYSICS, 44(6), pp.1041–1063. doi:https://doi.org/10.1190/1.1440994.

Tsuji, Y., Ishida, H., Nakamizu, M., Matsumoto, R., & Shimizu, S. (2004). Overview of the MITI Nankai Trough wells: A milestone in the evaluation of methane hydrate resources. *Resource Geology*, *54*(1), 3–10. doi:10.1111/j.1751-3928.2004.tb00182.x

Takashi, U., Lu, H. & Tomaru, H. (2004). Subsurface Occurrence of Natural Gas Hydrate in the Nankai Trough Area: Implication for Gas Hydrate Concentration. Resource Geology, 54(1), pp.35–44. doi:https://doi.org/10.1111/j.1751-3928.2004.tb00185.x.

Takashi, U., & Tsuji, T. (2004). Petrophysical properties of natural gas hydrates-bearing sands and their sedimentology in the Nankai Trough. *Resource Geology*, *54*(1), 79–87. doi:10.1111/j.1751-3928.2004.tb00189.x

Waite, W. F., Santamarina, J. C., Cortes, D. D., Dugan, B., Espinoza, D. N., Germaine, J., et al. (2009). Physical properties of hydrate-bearing sediments. *Reviews of Geophysics*, *47*(4), n/a-n/a. https://doi.org/10.1029/2008RG000279

Waite, W.P., R. Moerig & Hartmut Spetzler (1997). Seismic attenuation in a partially saturated, artificial crack due to restricted contact line motion. 24(24), pp.3309–3312. doi:https://doi.org/10.1029/97gl03308.

Walsh, J.B. (1965). The effect of cracks on the compressibility of rock. Journal of Geophysical Research, 70(2), pp.381–389. doi:https://doi.org/10.1029/jz070i002p00381.

Wood, W. T., Holbrook, W. S., & Hoskins, H. (2000). *In situ measurements of P-wave attenuation in the methane hydrate- and gas-bearing sediments of the Blake Ridge*. *Proceedings of the Ocean Drilling program, Scientific Results* (Vol. 164).

Zimmerman, R. W., & Kingt, M. S. (1986). The effect of the extent of freezing on seismic velocities in unconsolidated permafrost. *Geophysics*, *51*(6), 1285–1290. doi:10.1190/1.1442181

Yun, T. S., Francisca, F. M., Santamarina, J. C., & Ruppel, C. (2005). Compressional and shear wave velocities in uncemented sediment containing gas hydrate. *Geophysical Research Letters*, 32(10), 1–5. https://doi.org/10.1029/2005GL022607

Yun, T. S., Santamarina, C. J., & Ruppel, C. (2007). Mechanical properties of sand, silt, and clay containing tetrahydrofuran hydrate. *Journal of Geophysical Research: Solid Earth*, *112*(4), 1–13. https://doi.org/10.1029/2006JB004484

Zhan, L. (2020). ROCK PHYSICS STUDY ON THE FREQUENCY DEPENDENCE OF SEISMIC ATTENUATION IN METHANE HYDRATE-BEARING SEDIMENTS. Doctoral Thesis.

Zhan, L., & Matsushima, J. (2018). Frequency-dependent P-wave attenuation in hydrate-bearing sediments: a rock physics study at Nankai Trough, Japan. *Geophysical Journal International*, ggy229. doi:10.1093/gji/ggv229

Zhao, L. (2019). Dynamics and Statics of Three-Phase Contact Line. vtechworks.lib.vt.edu. [online] Available at: https://vtechworks.lib.vt.edu/handle/10919/102649 [Accessed 28 Jun. 2023].